Wake characteristics behind a tidal turbine with surface waves in turbulent flow analyzed with large-eddy simulation

Pablo Ouro [1,*] Hannah Mullings [1] Aristos Christou,[2]
Samuel Draycott [1] and Tim Stallard [1]

[1]*School of Engineering, University of Manchester, Manchester M13 9PL, United Kingdom*
[2]*Department of Civil, Environmental and Geomatic Engineering, University College London,
London WC1E 6BT, United Kingdom*

To design tidal stream turbine arrays, turbine wakes need to be fully characterized to assess the adequate row spacing considering environmental factors such as onset turbulence, velocity shear, and surface waves. The role of waves on wake development varies depending on their characteristics, such as wavelength and amplitude, and needs to be carefully understood. Here large-eddy simulations are performed to analyze the instantaneous and time-averaged wake characteristics developed downstream of a tidal stream turbine for four wave-current conditions ranging from nearly deep to intermediate waves and compared to current-only results. The tip-vortex convection near the free surface is highly influenced by the waves. During the period of increased surface elevation, there is an upwards motion of the vortices which have merged into a single vortical structure during the wave trough period. Downwards vertical transport of tip vortices occurs after the pass of the wave crest, enabling vertical entrainment of momentum into the turbine wake region. Disk-averaged velocity deficit recovery increases for wave-current cases compared to the current-alone condition, with all intermediate wave cases showing a very similar wake recovery rate throughout the wake length. The nearly deep-water waves lead to a slightly slower recovery rate up to 12 turbine diameters (D) downstream while, after this distance, the recovery rate is the highest among the simulated wave conditions. The integration of the mean kinetic energy (MKE) budget in the region up to $12D$ shows there is a similar distribution in the balance between terms irrespective of the wave-current case. However, in the far-wake region covering from $12D$ to $20D$, the nearly deep waves have a larger contribution for MKE replenishment from the transverse convection and turbulence transport terms, balanced with their vertical counterparts and the streamwise convection term. Analysis of the wake self-similarity shows that a Gaussian model description holds for the recovery rate and lateral profile of the wake of a tidal turbine operating in coupled wave-current conditions, with a similar rate of velocity recovery after $12D$ irrespective of the wave characteristics. Lateral wake spreading is smaller for the shortest wavelength, which relates to an increased contribution of transverse fluxes in the MKE budget.

*pablo.ouro@manchester.ac.uk

I. INTRODUCTION

Tidal stream energy is a growing offshore renewable energy technology that aims at capturing the kinetic energy from energetic tidal currents with either floating or bottom-fixed turbines. At most sites where tidal turbines are deployed or projected to be, there is a notable (stochastic) action of waves which is superimposed on the (predicted) tidal currents, which have a sheared profile and carries free-stream turbulence [1]. Depending not only on the wave characteristics, e.g., wavelength, amplitude, and steepness, but also the vertical velocity distribution and wave direction relative to the tidal flow, the role of waves in wave-current conditions varies [2]. Despite their importance to tidal stream turbine loading [3] and developed downstream wake [4], the research into the coupled action of waves and turbulent currents onto these devices has been limited [5], partly owed to the complexity of performing flow measurements and thus incomplete data to evaluate loading and wakes. The latter is needed as in open sea the decomposition of wave kinematics from acoustic Doppler current profiler data remains an open topic and waves are mostly irregular [6–8].

There has been a considerable amount of experimental work assessing the the effect of waves on tidal stream turbines with the majority focusing on the loading in regular wave conditions. These studies have tended to focus on the wave-induced variations in thrust and power (or torque) as a function of wave characteristics (e.g., Refs. [9–13]) along with comparisons of these to blade element momentum theory codes, e.g., Refs. [9,14,15]. Sensitivity has been conducted on the loading as a function of wave frequency and amplitude [10], wave phase [16], turbine depth [17], and turbine control strategy [18–20], among others. The loading on tidal stream turbines under regular wave conditions is therefore relatively well understood. These experimental findings on turbine loads have been further extended to cover irregular wave conditions [21–23] including understanding the role of rotational sampling on high-frequency blade loads [24] and the potential for extreme loads during large wave focusing events [25].

Despite the significant body of experimental work focused on loading behavior, only a few of these studies have concentrated on understanding the wake characteristics. In Stallard *et al.* [26], the role of opposing waves on the wave recovery behind a group of rotors was considered, finding that the velocity deficit in the near wake was reduced. Zhang *et al.* [27] performed an extensive experimental campaign with five wave-current conditions to explore their impact on the wake of a tidal turbine, noting a similar velocity deficit recovery between with and without wave cases, while demonstrating distinct turbulence intensity fields for the different wave cases. Zang *et al.* [28] analyzed the variation in power output and wake structure from a single tidal turbine in an experimental flume when this was subjected to current-only and wave-current conditions, showing a notable change in the power spectral density for the latter case. They also conclude that increasing wave height and length increases the wake recover rate. One of the challenges with all experimental studies is obtaining suitable velocity measurements. Single-point measurements from acoustic Doppler velocimeters are almost exclusively used for these analyses and hence instantaneous spatial measurements are not possible, and the spatial range and resolution often limited.

To date, numerical studies using CFD have mostly looked at the impact of waves on the loading and wakes of tidal turbines with RANS turbulence closures but neglecting the role of turbulence. Tatum *et al.* [29,30] simulated how surface waves and a sheared velocity profile alters the distribution of thrust and bending moments over the turbine rotation but without characterizing the downstream wake. Apsley *et al.* [31] performed RANS simulations with actuator line model for two wave-current interaction cases varying the wavelength, and observed the large variation in power coefficient depending on the wave characteristics. Through unsteady RANS simulations, Li *et al.* [32] observed that surface waves modulate the turbine wake dynamics for wave-current conditions through instantaneous velocity contours and analysis with proper-orthogonal decomposition.

While the previous RANS-based studies have proven essential to further elucidate how waves impact tidal turbine wakes and loading, these do not yield sufficient accuracy to capture the complexity of the instantaneous flow field in presence of flow turbulence, velocity shear, and surface waves. Thus, high-fidelity turbulence closures, e.g., large-eddy simulation, need to be adopted

[33–35]. Stallard *et al.* [36] compared the wake characteristics of a single laboratory-scale turbine in current-only and one wave-current condition for a nearly deep wave. This study showed that waves accelerated disk-averaged velocity recovery and modified the vertical wake structure near the free surface. The present study expands on this with an in-depth analysis of the wake structure behind a single tidal stream turbine with identification of the driving physics for four wave-current conditions.

The paper is structured as follows: The current-only and wave-current cases simulated are introduced in Sec. II while the governing equations used in the LES framework and numerical setup are discussed in Sec. III. Results are presented in Sec. IV, including the instantaneous turbulent flow field obtained from LES for the different wave conditions, time-averaged mean velocity and velocity fluctuation, and quantification of the mean kinetic energy budget to determine the sources contributing to the recovery of momentum in the wake. Finally, the main findings are discussed in the Conclusions.

II. CASES DESCRIPTION

The experimental setup from a previous testing campaign by Stallard *et al.* [26] is adopted in the large-eddy simulations. The recirculating open-channel facility is 12.5 m long and 5 m wide, with the mean water depth (h) equal to 0.45 m. The velocity at the turbine position featured a logarithmic vertical distribution [$U(z)$] with depth-averaged value (U_0) of 0.47 m/s and friction velocity (u_*) of 0.0187 m/s, defined as,

$$\frac{U(z)}{u_*} = \frac{1}{\kappa}\ln\left(\frac{zu_*}{\nu}\right) + C,$$ (1)

where κ is the von Karman constant equal to 0.41, ν is the kinematic viscosity of the fluid set to 1×10^6 m^2/s, z is the vertical coordinate, and C is a constant equal to 5 according to open-channel flows over rough beds. The bulk Froude number (Fr $= U_0/\sqrt{gh}$, with g being the gravity acceleration) is 0.224 and bulk Reynolds number (Re $= U_0h/\nu$, with ν indicating the kinematic viscosity of the water) of 1.27×10^5. Note that no waves were considered in these experiments. The integral turbulence lengthscales measured in the flume were $0.56h$, $0.33h$, and $0.25h$, in streamwise, transverse, and vertical directions, with a mean streamwise turbulence intensity of 10% measured at 6 m downstream of the flume's inlet and of 8% at 3 m further downstream [26].

A single horizontal axis tidal stream turbine with three blades whose hydrodynamic sections were Göttingen 804 (with lift and drag coefficients provided in Stallard *et al.* [26]) and a diameter (D) equal to 0.27 m is modelled, operating at its peak performance operating point corresponding to a tip-speed ratio ($\lambda_t = \Omega_t D/2U_0$, with Ω_t being the turbine rotor's rotational speed) of 4.5, i.e., it rotates at an angular speed $\Omega_t = 15.33$ rad/s. At this rotational speed, the turbine's rotor rotational period is $T = 0.41$ s and the blade passing period $f_b = 0.137$ s. The turbine had a nacelle that spans 0.09 m in the x direction with a diameter of 0.01 m, and a circular vertical support structure whose diameter was 0.015 m and connected the turbine's hub to the supporting frame placed above the water surface [26].

In this study, four wave characteristics are chosen, keeping the same wave height (H) of 0.05 m, that span from nearly shallow wave conditions (one case), two intermediate waves, and one deep water wave. These four wave characteristics cover a wide range of wave-depth parameters for the selected wave amplitude to enable understanding of the action of following waves on tidal turbine wakes. Further details provided in Table I including waves' characteristics (wavelength λ_w, period T_w, and frequency f_w), wavelength-to-turbine diameter ratio (λ_w/D), nondimensional depth (kh), ratio between blade passing frequency of the turbine to the wave frequency (f_b/f_w), and wave steepness ($kH/2$).

TABLE I. Details of the wave-current cases simulated including wavelength (λ_w), wave period (T_w), wave frequency (f_w), wavelength to turbine diameter ratio (λ_w/D), wave-depth parameter (kh), ratio of blade passing frequency to wave frequency (f_b/f_w), and wave steepness ($kH/2$).

Case	λ_w (m)	T_w (s)	f_w (Hz)	λ_w/D	kh	f_w/f_b	$kH/2$
1	1	0.58	1.710	3.7	2.827	4.27	0.1570
2	2.89	1.25	0.800	10.7	0.978	9.15	0.0544
3	4	1.65	0.605	14.8	0.707	12.10	0.0393
4	8	3.16	0.316	29.6	0.353	23.16	0.0196

III. NUMERICAL FRAMEWORK

This section describes the in-house numerical solver which adopts large-eddy simulation to resolve the flow field, an actuator line method to represent the rotating turbine blades, a direct-forcing immersed boundary method to account for the turbine's support structure and hub, and a level-set method to represent the air-water interface and thus model waves using second-order Stokes theory. All is implemented in a fully parallel environment to efficiently compute simulations on thousands of cores.

A. Computational model

The in-house code digital offshore farms simulator (DOFAS) [37] is used to perform large-eddy simulations of open-channel flows with surface waves, which adopts a level-set method (LSM) for the wave generation and an actuator line model (ALM) for the turbine rotor representation. DOFAS is built onto the fluid solver Hydro3D [38,39], which offers excellent scalability behavior on high-performance computing facilities [40] when conducting massive parallel simulations, as it is fully parallelized with message passing interface [41] and OpenMP [42]. The code has successfully been used in a number of complex computational studies in the fields of traveling free-surface waves [43,44], turbulent free-surface flows [45–48] and in pipe flows [49], sediment transport [50], or flow over rough bathymetry [51–53], among others. DOFAS has also been extensively validated and applied to tidal stream turbines at individual [36,54,55] and array levels [37,56], providing turbine load prediction in complex flows [57–59], analysis of wake recovery mechanisms [60], and real multirow array micrositing [61].

DOFAS resolves the spatially filtered Navier-Stokes equations for incompressible flow using a filter size equal to the grid size with staggered storage of velocities in a rectangular Cartesian grid. The latter is divided into rectangular subdomains that are mapped to the processors adopted to run the simulation. The code resolves the LES turbulence closure in which the energetic flow structures are explicitly resolved while the small-scale turbulence is modelled using a subgrid scale model [62]. The wall-adapting local eddy-viscosity subgrid scale model from Nicoud *et al.* [63] is employed to compute the effects of the unresolved small-scale turbulence. The governing equations resolved by DOFAS are as follows:

$$\frac{\partial u_i}{\partial x_i} = 0, \qquad (2)$$

$$\frac{\partial u_i}{\partial t} + \frac{\partial u_i u_j}{\partial x_j} = -\frac{1}{\rho}\frac{\partial p}{\partial x_i} + \nu\frac{\partial^2 u_i}{\partial x_j \partial x_j} - \frac{\partial \tau_{ij}}{\partial x_j} + f_i + g_i, \qquad (3)$$

where u_i and u_j are the resolved velocity components (i or $j = 1, 2$, and 3, which denote the x, y, and z directions, respectively), x_i and x_j represent the spatial coordinate components in the three spatial directions, ρ is the density of the fluid, p is the resolved pressure, ν is the kinematic viscosity of the fluid, τ_{ij} are the subgrid scale stresses, f_i represents external forces calculated using the actuator

line method for the turbine blade action or immersed boundary direct forcing method [64] for the turbine's hub and support structure, and g_i is the gravitational acceleration.

A fractional step method is employed to advance the simulation in time using a three-step low-storage Runge-Kutta scheme with a multigrid method for the resolution of the Poisson pressure equation. The diffusive terms in the Navier-Stokes equations are approximated by second-order central differences, while convective velocity fluxes in the momentum conservation equation and the advection equation from the level-set method are approximated using a fifth-order weighted essentially nonoscillatory (WENO) scheme. The main advantage of the WENO scheme is its capability to achieve the necessary compromise between numerical stability and physical accuracy when simulating two-phase flows [40].

The LSM [65] is adopted to resolve the free surface between the air and water phases. The LSM employs a level-set signed distance function, ϕ, with positive values of ϕ denoting water, whereas $\phi \leqslant 0$ corresponds to the air. The air-water interface corresponds to a zero value of ϕ. The LSM is resolved adopting a three-step total-diminish variation Runge-Kutta to compute the signed distance function ϕ, with a fifth-order WENO method to approximate the fluxes in the center of the grid cells [40]. The spatial evolution of the ϕ function is tracked over time by solving a pure advection equation:

$$\frac{\partial \phi}{\partial t} + u_i \frac{\partial \phi}{\partial x_i} = 0. \tag{4}$$

Due to the inherent nature of the advection equation, mass conservation is not ensured, as the required numerical stability criterion of $|\nabla \phi| = 1$ is not directly satisfied. Therefore, LSM is re-initialized to ensure that this criterion is fulfilled at every time step, so that mass is conserved in the computational domain [66].

A Heaviside function [$\mathscr{H}(\phi)$, Eq. (5)] is applied at the air-water transition to allow a smooth transition between the two immiscible fluids [40,43] and avoid potential numerical instabilities due to any sudden change in density (ρ) and viscosity (μ). The transition region between phases has a width equal to $2.0 \cdot \Delta x_i$ [67], which adjusts the thickness of the numerical smearing at the interface,

$$\mathscr{H}(\phi) = \begin{cases} 0 & \text{if } \phi < -2.0 \cdot \Delta x_i \\ \frac{1}{2} + \frac{1}{2}\left[\frac{\phi}{2.0 \cdot \Delta x_i} + \frac{1}{\pi}\sin\left(\frac{\pi\phi}{2.0 \cdot \Delta x_i}\right)\right] & \text{if } |\phi| \leqslant 2.0 \cdot \Delta x_i \\ 1 & \text{if } \phi > 2.0 \cdot \Delta x_i \end{cases} . \tag{5}$$

Finally, the density and dynamic viscosity fields are calculated as

$$\begin{aligned} \rho(\phi) &= \rho_a + (\rho_w - \rho_a)\mathscr{H}(\phi) \\ \mu(\phi) &= \mu_a + (\mu_w - \mu_a)\mathscr{H}(\phi), \end{aligned} \tag{6}$$

where the subscripts w and a represent water and air, respectively.

The wave generation and absorption methods are presented and validated in Christou *et al.* [43] with a short description provided here. At the inlet, unidirectional following wave conditions are generated imposing Dirichlet boundary conditions to the free-surface level (η) and velocity components in streamwise and vertical directions, which are then superimposed onto the mean velocity profile [$U(z)$] and artificial turbulence [$u'_{i,\text{SEM}}(x = 0, t)$] with synthetic eddy method (SEM) [68]. In this work, second-order Stokes wave theory [44] is adopted to generate the wave elevation and kinematics as a function of their relative depth and wave steepness, as shown in Table I. In these wave-current conditions, the dispersion relation used to obtain the wave angular frequency in the fixed reference frame (ω_w) takes into account the relative wave frequency $\omega_r = gk \tanh(kh)$ with the convective velocity (U_0) being the bulk (depth-averaged) velocity and reads:

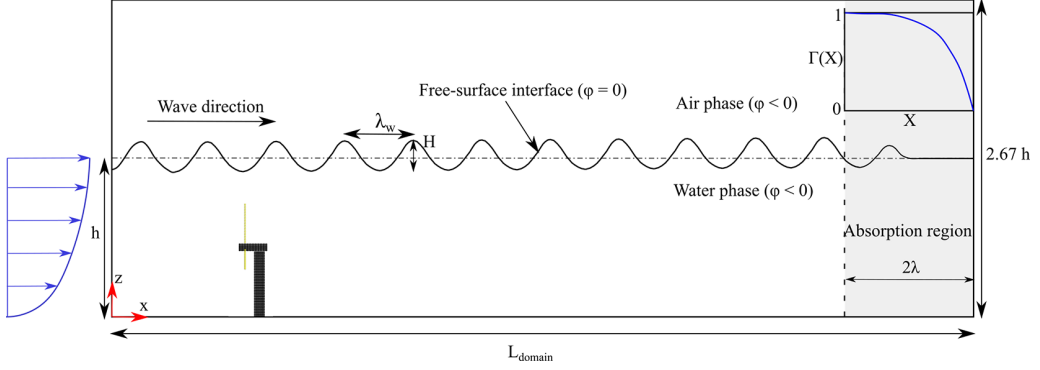$$(\omega_w - kU_0)^2 = gk \tanh(kh). \tag{7}$$

FIG. 1. Schematic of the computational domain adopted for the large-eddy simulations of the horizontal axis tidal turbine operating in an open-channel flow with waves. The total length of the domain is L_{domain}, mean water depth is denoted as h, and wave height and length are H and λ_w, respectively. An absorption region of length $2\lambda_w$ is set at the outlet of the domain to absorb waves and avoid their reflection.

The free-surface elevation referenced from the bed ($z = 0$) is computed accordingly to:

$$\eta(x = 0, t) = h + \frac{H}{2}\cos\left(\omega_w t - \frac{\pi}{2}\right) + \frac{H^2 k}{16}[3\coth^3(kh) - \coth(kh)]\cos\left[2\left(\omega t - \frac{\pi}{2}\right)\right]. \quad (8)$$

Velocity components are prescribed at the inlet ($x = 0$), with the vertical origin of coordinates at the bed ($z = 0$), as:

$$u(x = 0, t) = \bar{U}(z) + u'_{\text{SEM}} + \frac{H}{2}\omega_r\left[\frac{\cosh(kz)}{\sinh(kh)}\right]\cos\left(\omega_w t - \frac{\pi}{2}\right)$$

$$+ \frac{3}{16}\omega_r(kH)^2\left[\frac{\cosh(2kz)}{\sinh^4(kh)}\right]\cos\left[2\left(\omega t - \frac{\pi}{2}\right)\right], \quad (9)$$

$$w(x = 0, t) = w'_{\text{SEM}} - \frac{H}{2}\omega_r\left[\frac{\sinh(kz)}{\sinh(kh)}\right]\sin\left(\omega_w t - \frac{\pi}{2}\right)$$

$$- \frac{3}{16}\omega_r(kH)^2\left[\frac{\sinh(2kz)}{\sinh^4(kh)}\right]\sin\left[2\left(\omega t - \frac{\pi}{2}\right)\right]. \quad (10)$$

At the outlet, a relaxation method is used to absorb the waves and avoid their reflection, which gradually decreases the velocities and signed-distance function of the LSM to approach the target values, e.g., those imposed at the inlet. The relaxation function Γ reads [44]:

$$\Gamma(X) = 1 - \frac{e^{X^{3.5}} - 1}{e - 1}, \quad (11)$$

where the nondimensional coordinate X has values in the range of [0,1] and is defined as:

$$X = \frac{x - x_s}{x_e - x_s}, \quad (12)$$

where the denominator $(x_e - x_s)$ represents the length of the absorbing layer, set for each of the wave cases to twice the wavelength, i.e., $2\lambda_w$, where x_e is the domain's outlet coordinate and $x_s = x_e - 2\lambda_w$ the start of this region.

B. Computational setup

The computational domain, presented in Fig. 1, is set up considering three criteria: At least two wavelengths are kept between the inlet and turbine position, two wavelengths are used for the relaxation region at the downstream end, and at least six wavelengths can be developed in the turbine wake region to fully capture their interaction. Based on these criteria, the numerical domain measures 40, 3, and 1.2 m in the streamwise, transverse, and vertical directions for wavelengths of 4 m and smaller. This is greater in length than the experimental open-channel facility (12.5 m) to ensure that no wave reflection from any boundary occurs while it is narrower in its transverse dimension to reduce computing cost with the lateral global blockage still low, namely 4.25%. In the case with the longest wavelength ($\lambda_w = 8$ m, $kh = 0.353$), the domain is doubled in length to 80 m so the above criteria are met.

As per the velocity boundary conditions, the logarithmic distribution of velocities measured in the experiments from Stallard *et al.* [69] is set at the inlet and heterogeneous isotropic artificial turbulence generated with the SEM superimposed, with the turbulence intensity and lengthscales equal to those measured in the experiments. Wave-induced velocities at the inlet are also linearly superimposed, noting that herein the wave direction is aligned with flow, while in the experiments from Stallard *et al.* [26] wave direction was opposed to flow with comparable kh. On the lateral boundaries, periodic conditions are imposed while at the bottom wall, a hydraulically smooth wall function is adopted, as the vertical grid resolution in wall units is 42. At the outlet, a Neumann boundary conditions is imposed to the velocities.

A uniform grid resolution of $\Delta x_i = 0.005$ m is used throughout the domain to ensure the air-water interface, waves, and turbulence are well resolved everywhere. With this grid size, there is a total of 54 mesh elements across the turbine diameter which is enough to capture the tip vortices and other wake dynamics [37]. This leads to a total number of grid cells of 1.152×10^9. The time step is kept fixed at $\Delta t = 0.001$ s. The same setup but with shorter domain in current-only conditions was adopted in Ouro *et al.* [37] to validate DOFAS's predictions in terms of turbine wake hydrodynamics and loading. Simulations run using 8000 CPUs on the UK national supercomputing facility ARCHER2, for the smaller domain, while 16 000 CPUs are adopted for the longest wavelength case, all requiring 144 h of compute time. A total physical time of 400 s is run for every simulation, with first-order statistics collected after discarding the first 50 s of simulation and turbulence statistics captured after the first 150 s, therefore averaged over 250 s in total.

The turbine is placed at 8.36 m (18h or approximately $2\lambda_w$, $2.9\lambda_w$, and $8\lambda_w$ for the cases with $kh = 0.707$, 0.978, and 2.827, respectively) from the inlet for the three shortest wavelengths (as h/H is constant) conditions while this distance is doubled to 36h for the longest wavelength case (to ensure two wavelengths are developed between the turbine and inlet). The hub height is at 0.225 m ($h/2$), as in the experiments and centered in the transverse dimension of the numerical domain, which is at midwater depth, leaving a clearance between top blade tip (0.36 m) and mean water level (h) of 0.09 m, i.e., 0.2h. Both nacelle and supporting structures are included in the model and resolved with the immersed boundary method, with the latter extending between the hub height and bottom bed and not piercing through the free surface as in the experiments in order to avoid any further interaction with the waves.

The Reynolds decomposition is used to compute the time-averaged mean velocity U_i and fluctuating velocity u_i', as $u(t) = U_i + u_i'(t)$. Note that for the current-only case, the fluctuating velocity is analogous to the turbulent velocity fluctuation. However, in this study for the wave cases no decomposition to the fluctuating velocity is done in terms of turbulence and wave-induced unsteadiness. Thus, for convenience, the term u_i' is referred to as velocity fluctuation term and the so-called Reynolds stresses in no-wave cases, i.e., $u_i'u_j'$, are the cross-correlation of fluctuating velocity components. For convenience, disk-averaged values are denoted as $\langle \cdot \rangle$.

IV. RESULTS

In this section, the effect of waves on the wake structure of a single tidal stream turbine is analyzed. First, the instantaneous flow structures are visualized as contours of spanwise vorticity through a wave cycle across a vertical plane through the rotor axis, followed by a comprehensive study of the time-averaged wake statistics in terms of velocity and Reynolds stresses. Finally, the streamwise evolution of the disk-averaged velocity and mean kinetic energy budget terms are presented.

A. Instantaneous wake structures

Periodic regular surface waves introduce a source of velocity intermittency that impacts the interaction of the turbine-induced wake and flow structures within the ambient flow. Thus, the role of waves on tidal turbine hydrodynamics is first discussed, looking at the spatiotemporal evolution and spatial correlation of the flow structures, mainly tip vortices, and how they are convected downstream of the turbine.

The instantaneous flow field computed for the current-only case, i.e., without waves, is presented in Fig. 2 showing contours of spanwise vorticity over a vertical plane across the center of the turbine during four time intervals spaced $T_w/4$ in time (approximately 0.5 turbine's rotor revolutions or 1.5 blade passes). Over these time frames, the tip vortices travel over the horizontal projection of the top blade tip over most of the wake region shown. They are coherent and can be individually identified up to $x/D = 1$, when they roll up into larger structures of 2–3 times their size. After $x/D \geqslant 3$, the tip vortices are seen to lose coherence and mix with the rest of the smaller-scale flow structures.

Surface waves change the flow field immediately downstream of the turbine and its near-wake distribution. Figure 3 presents the contours of vorticity for the case of the longest waves modelled ($kh = 0.353$) for four consecutive time intervals spaced $T_w/4$ (approximately 1.5 turbine's rotor revolutions) to enable coverage of the full wave period. In this wave-current condition, the tip vortices remain coherent for a large streamwise distance compared to the intermediate (Figs. 4 and 5) and deeper (Fig. 6) wave cases due to the different wave phase and hence variations in wave-induced velocity. Figures 3(a) corresponds to an instant in time when the wave trough is at the turbine position, in which tip vortices are convected mostly horizontally. During the zero-upcrossing of these long waves, Figs. 3(b) and 3(c), the larger roll-up vortex moves upwards and the larger wave period allows for these energetic flow structures to remain near the free surface for a longer streamwise distance. Figure 3(d) presents a snapshot during a period of decreased surface elevation, with the remnants of the tip vortices traveling well above the blade's top-tip height after $x/D > 2$ which will entrain the wake region as the wave crest reaches their downstream location.

Visualization of these vortical structures for the wave case with $kh = 0.707$ is presented in Fig. 5, with the four snapshots advancing $T_w/4$ in time between each of them to enable depiction of the full wave period. In Fig. 5, tip vortices appear below the top-tip location as the wave trough is above the turbine location. The following wave zero up-crossing induces a large disturbance to the tip vortices with an upwards motion which is highlighted in Fig. 5(c), showing the roll-up motion of the vortices during their convection and approximation to the free surface. Once the wave crest passes the turbine location, and the decrease in wave elevation starts, the negative vertical velocity through zero down-crossing and negative wave-induced horizontal velocity under the trough leads the tip vortices to eventually travel in a downwards motion as the following wave trough approximates the turbine rotor again.

Results for the case with waves $kh = 0.978$, shown in Fig. 5, show a similar behavior of the turbine wake flow structures to $kh = 0.707$, i.e., tip vortices are coherent within the region $0 \leqslant x/D \leqslant 1$, after which they merge into larger flow structures. In both Figs. 4 and 5, tip vortices are seen to slightly interact with the waves with free-surface elevation alterations observed even up to $4D$ downstream of the turbine.
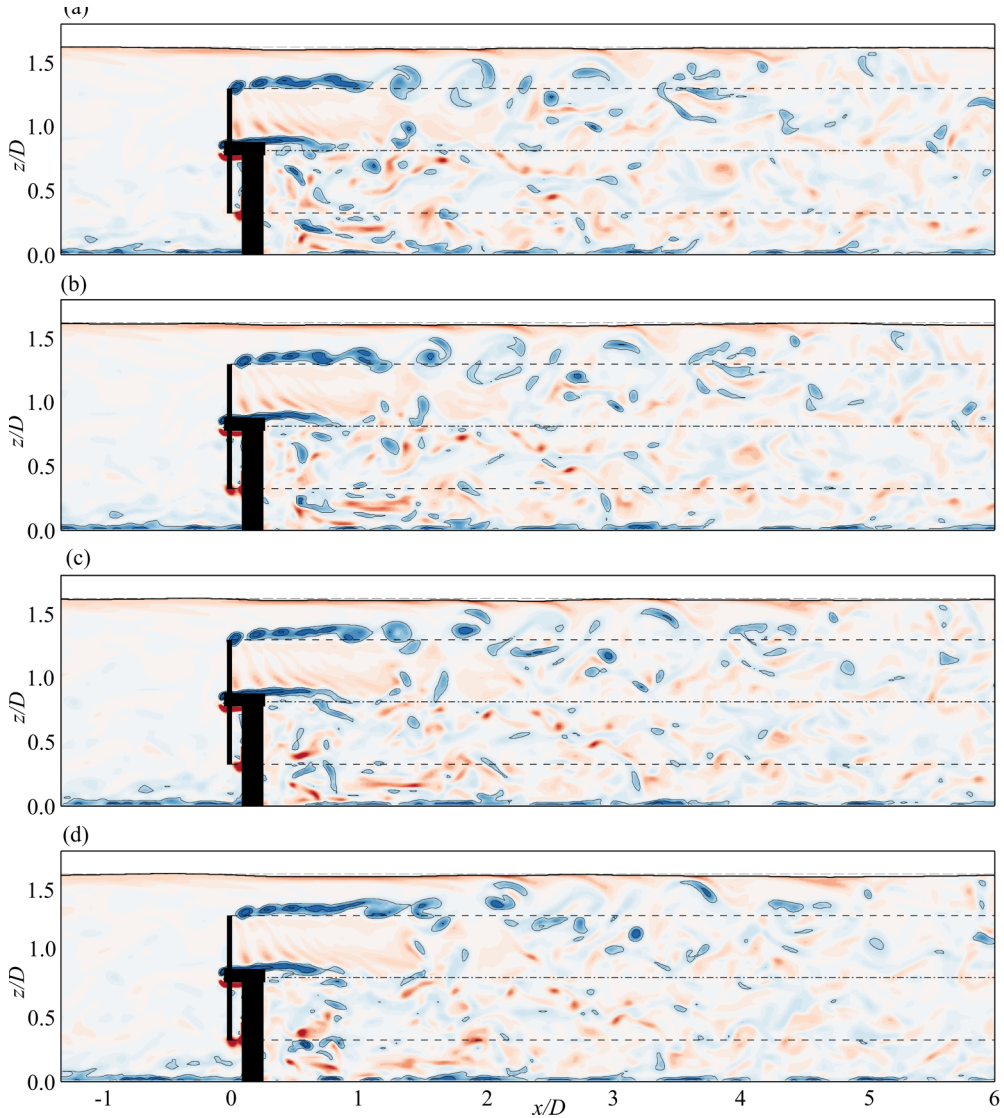
FIG. 2. Contours of normalized spanwise vorticity (Ω_y) over a xz plane at $y/D = 0$ for the current-only case. Time snapshots are equally spaced at increments of $T_w/4$.

Figure 6 presents the contours of vorticity during four snapshots for the case with waves of $kh = 2.827$, which approach deep-water wave conditions ($kh \geqslant \pi$) and for which the near-bed wave-induced velocity is approximately 0. Several substantial differences can be observed to the near-wake region due to the presence of the waves, changing the path followed by the tip vortices once shed by the blades. When the wave trough is at the rotor position, the tip vortices are pushed down and move below the top-tip blade location. During the zero up-crossing, wave-induced vertical velocity is maximum leading to an upwards motion of these vortices which remain coherent in the very-near wake region ($x/D \leqslant 1$). This latter tip-vortex movement over the turbine top-tip location remains until the wave crest passes the turbine location, as seen in Fig. 6(c). During the zero down-crossing motion of these short waves, the tip vortices travel downwards. Hence, waves are seen to drive the streamwise transport of turbine-induced flow structures. The vertical range over which vertical mixing occurs also increases with lower kh.
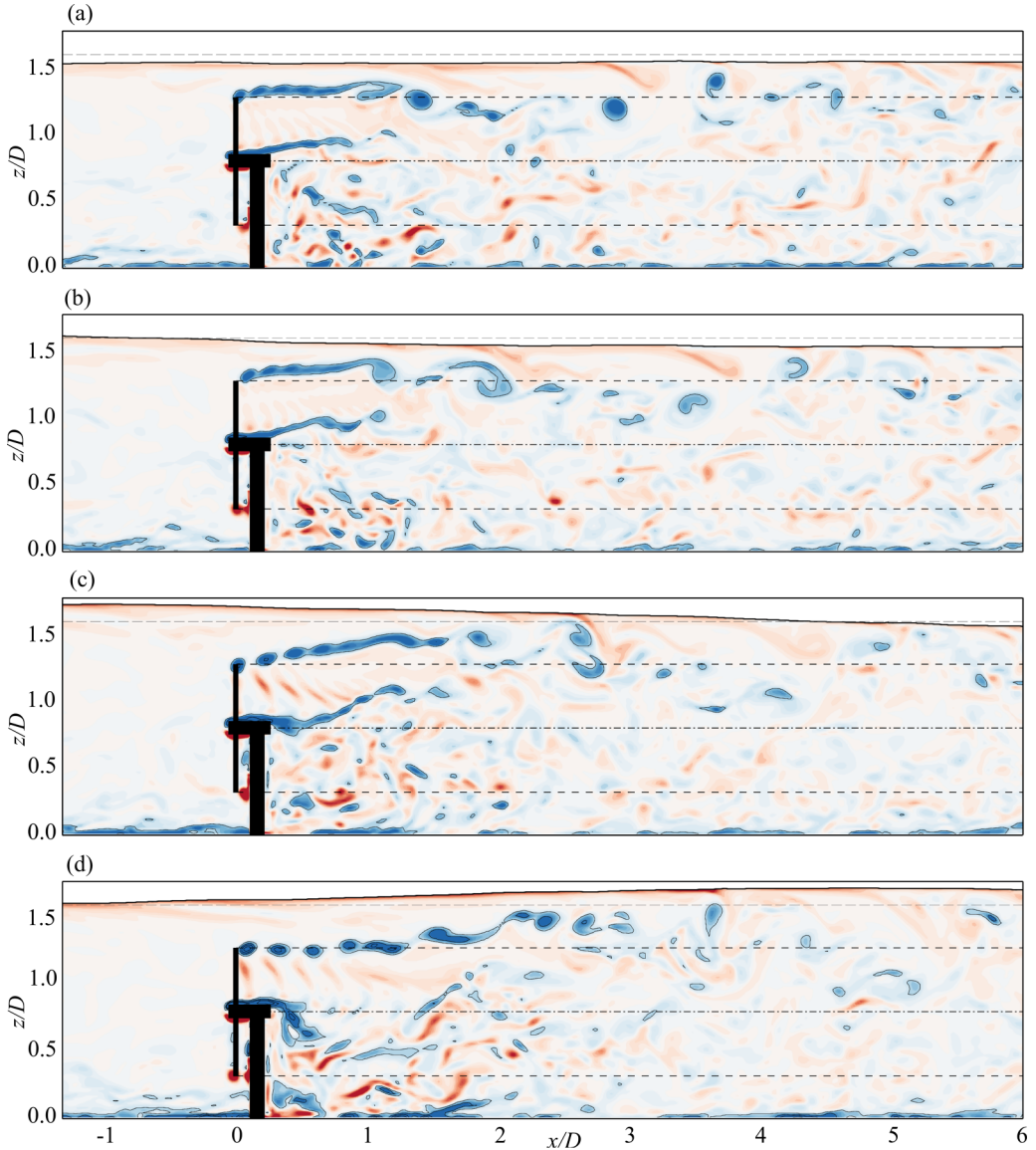
FIG. 3. Contours of normalized spanwise vorticity (Ω_y) over a xz plane at $y/D = 0$ for wave case with $kh = 0.353$. Time snapshots are equally spaced at increments of $T_w/4$.

Overall, Figs. 2–6 outline that waves impact the vertical and streamwise transport of the tip vortices with a periodic action. The frequency of the upwards motion of tip vortices sweeping away from the top-tip height towards the free surface during the $\partial\eta/\partial t > 0$ period, and their downwards motion entraining again into the wake region will drive the wake dynamics as shown in the next section.

The spatial coherence of the top tip vortices convection seen in the instantaneous flow field contours is further investigated with the computation of the two-point correlation over a period of approximately 400 turbine revolutions (164 s of physical time) with flow data stored every 0.1 s (one quarter of turbine revolution). The cross-correlation of velocities between two points (R_{uu}) is
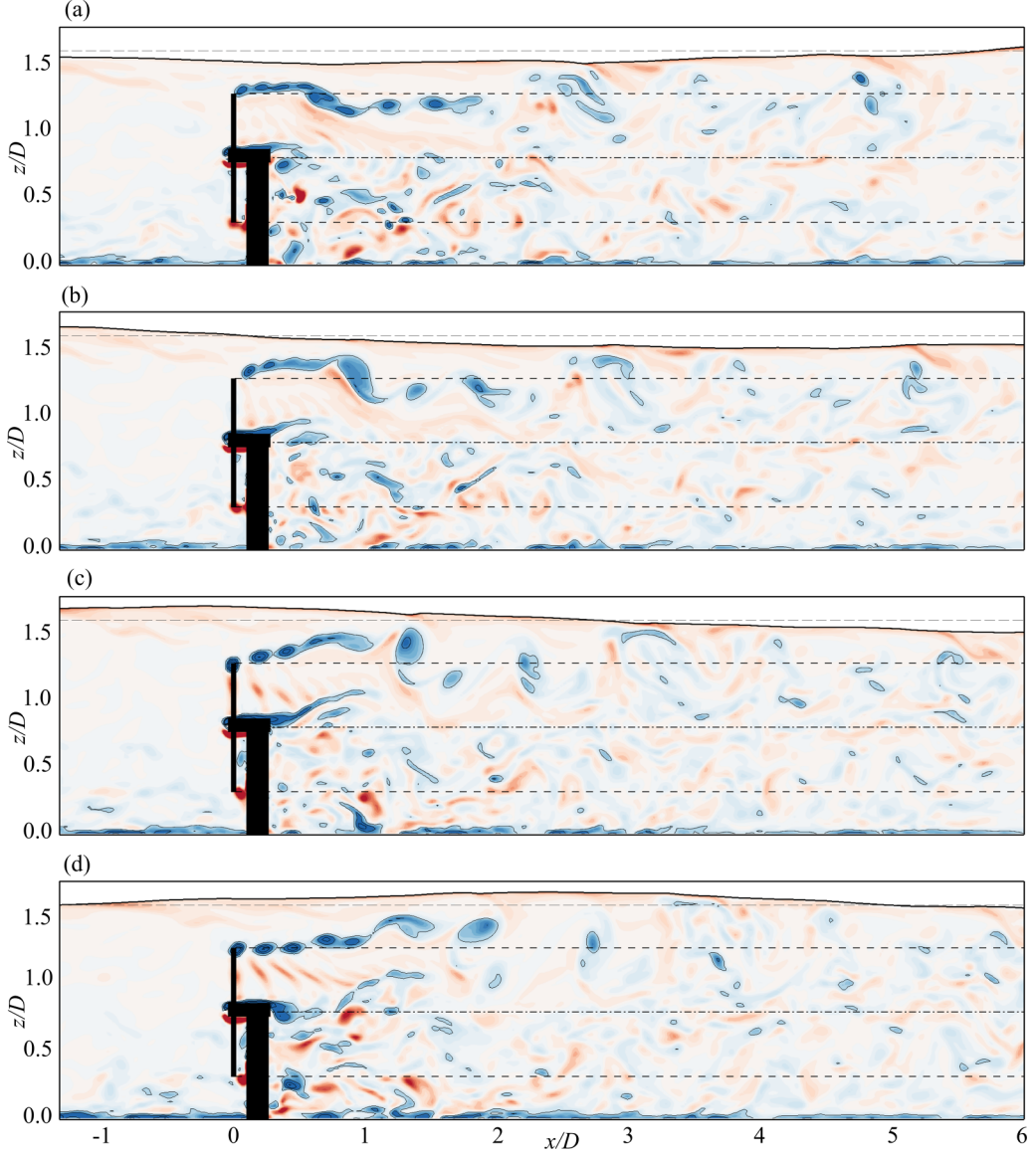
FIG. 4. Contours of normalized spanwise vorticity (Ω_y) over a xz plane at $y/D = 0$ for wave case with $kh = 0.707$. Time snapshots are equally spaced at increments of $T_w/4$.

defined as:

$$R_{u_i u_j}(\mathbf{x}_{\text{ref}}, \mathbf{x}_n) = \frac{\overline{u_i(\mathbf{x}_{\text{ref}}, t) \cdot u_j(\mathbf{x}_n, t)}}{\sqrt{\overline{u_i(\mathbf{x}_{\text{ref}}, t)^2} \cdot \overline{u_j(\mathbf{x}_n, t)^2}}}, \tag{13}$$

where ($\bar{\cdot}$) indicates time-averaging operation, $\mathbf{x}_n$ is the spatial coordinates of cell n, while $\mathbf{x}_{\text{ref}}$ is that for the adopted reference point. As reference location, the coordinates at $x/D = 2$ and $z/D = 1.33$ are considered as this location coincides with the downstream projection of the top-tip blade location where tip vortices travel through during their upwards and downwards motion due to wave action. Results of the two-point correlation are shown in Fig. 7. For the current-only and longest wave cases
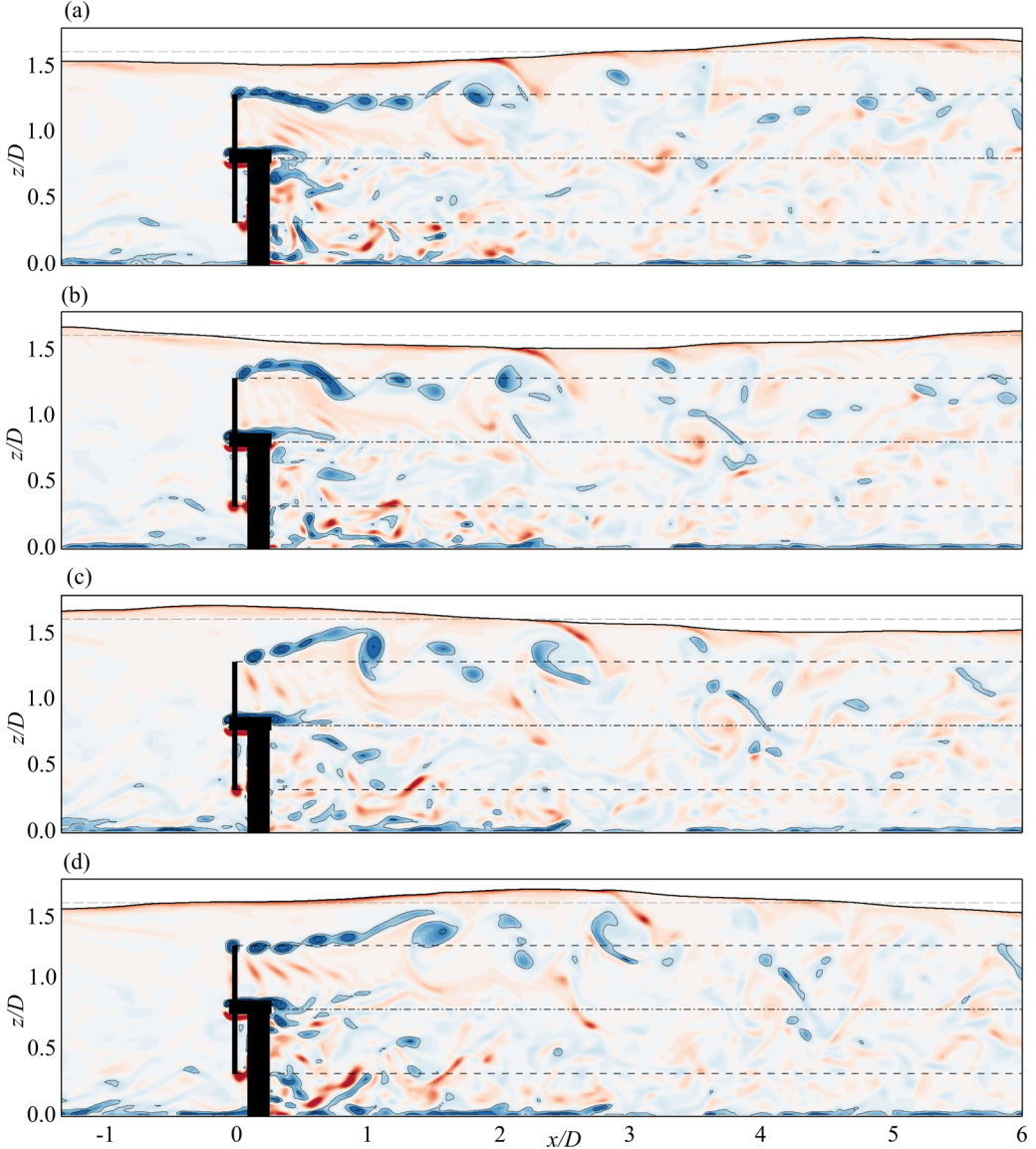
FIG. 5. Contours of normalized spanwise vorticity (Ω_y) over a xz plane at $y/D = 0$ for wave case with $kh = 0.978$. Time snapshots are equally spaced at increments of $T_w/4$.

($kh = 0.353$), there is only a small spatial region featuring a high correlation with the reference point, while for the intermediate wave cases this expands over larger areas of high correlation, both positive and negative. For the $kh = 2.827$ case [Fig. 7(e)] there is a positive correlation with the area enclosing the reference point and expanding vertically, which alternates with regions of limited negative correlation shortly before and after the reference point in the streamwise direction. Correlation with other regions closer to the turbine are seen at $x/D = 1.2$–1.7 ($R_{uu} > 0$) and before at $x/D = 0.8$–1.2 ($R_{uu} < 0$). These alternate positive-negative correlation to the reference point is a signature of a general repeating correlation oscillating pattern every wavelength from the wave-induced velocities seen in Fig. 6. Further downstream at $x/D \geqslant 3$, larger areas showing negative ($3 < x/D < 4$) and positive ($5 < x/D < 6$) correlation result from the time phase between tip-vortex
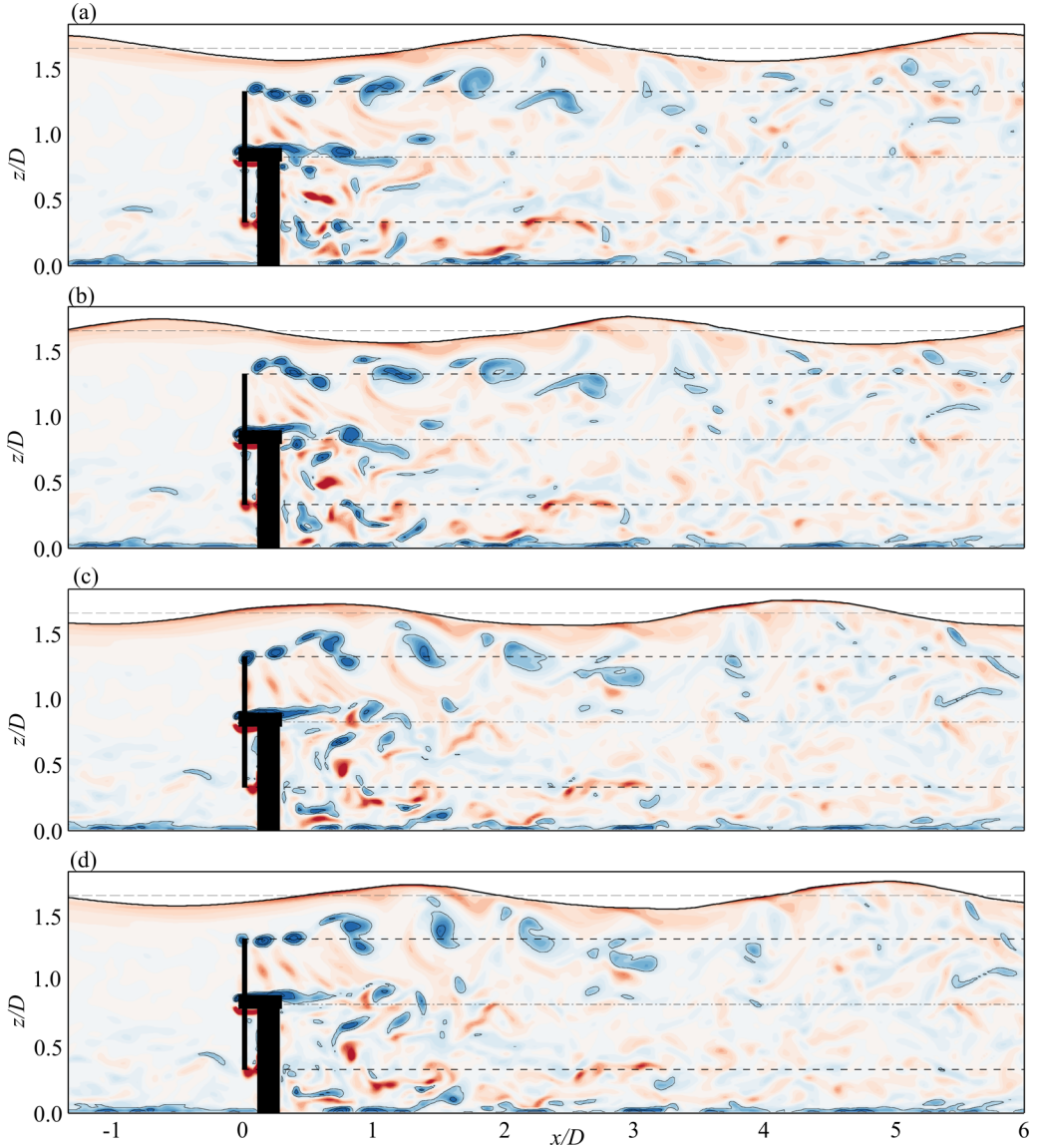
FIG. 6. Contours of normalized spanwise vorticity (Ω_y) over a xz plane at $y/D = 0$ for wave case with $kh = 2.827$. Interval time between snapshots is constant and equal to $T_w/4$.

convection and velocity-induced by surface waves. Results of R_{uu} for $kh = 0.978$ and 0.707 in Figs. 7(c) and 7(d) show a similar distribution of alternative highly correlated regions but occupying a larger streamwise and vertical region when compared to that of $kh = 2.827$.

Figure 8 presents the power spectral density (PSD) of the streamwise velocity fluctuations, which have been computed at the point indicated in the two-point correlation (Fig. 7). The PSD of the streamwise velocity fluctuation show energy peaks for the wave frequencies, with the width of these high spectral energy regions increasing as kh decreased. The spectrum of the current-only case features a $-5/3$ in the inertial range followed by a $-11/3$ in the dissipation range [70], which is kept in the wave-current cases. This suggests that waves do not significantly impact the energy cascade of the turbulent structures, neither the large scales nor the smallest, isotropic ones.
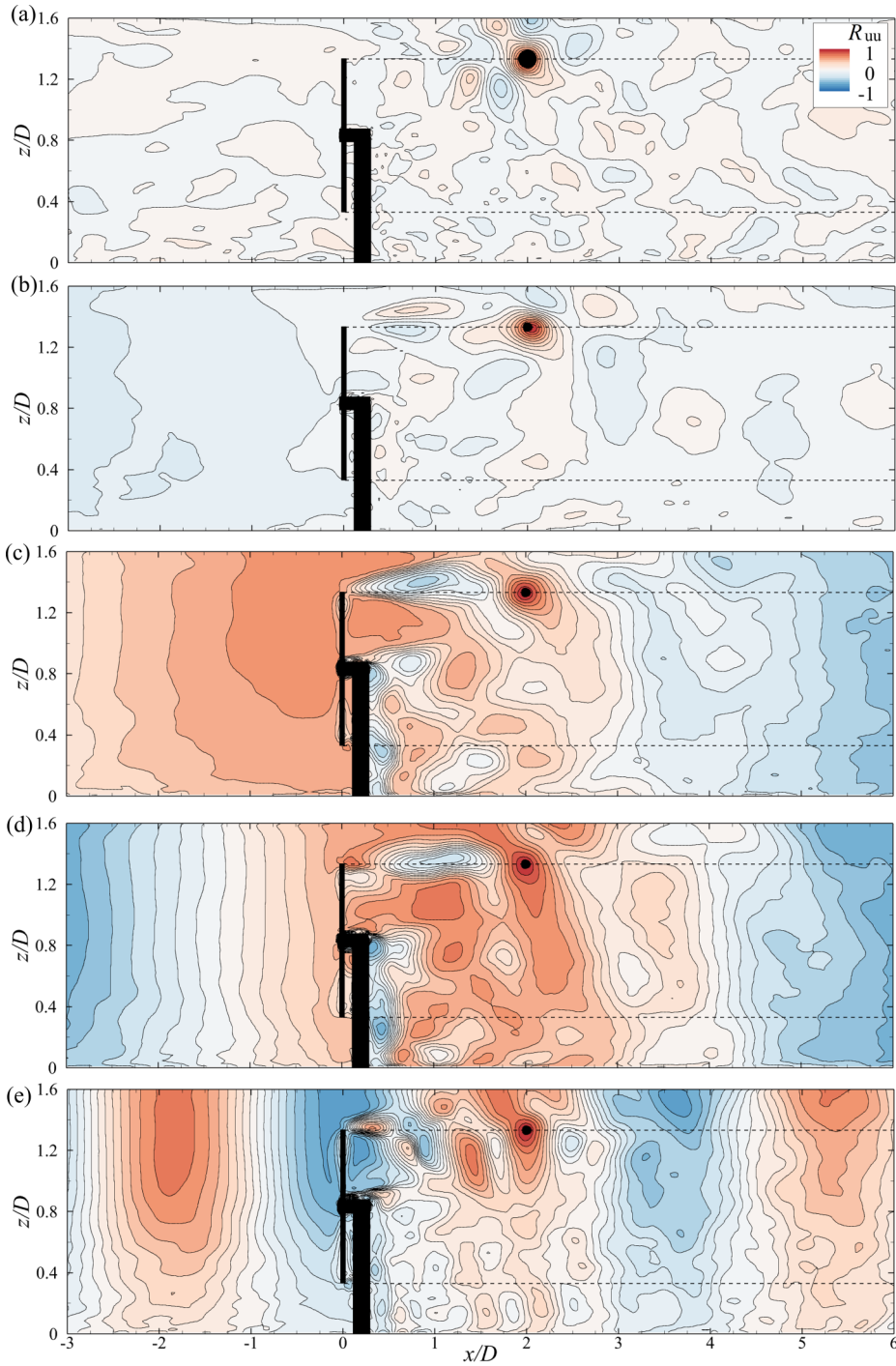
FIG. 7. Contours of two-point correlation of the streamwise velocity (R_{uu}) over a xz plane at $y/D = 0$ for the cases simulated. Reference point is taken at the top blade tip position two diameters downstream of the turbine's rotor. Results from the (a) no wave, (b) $kh = 0.353$, (c) $kh = 0.707$, (d) $kh = 0.978$, and (e) $kh = 2.827$.
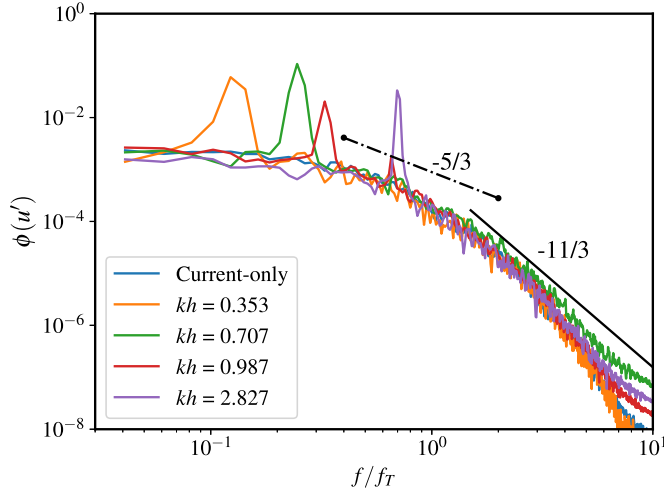
FIG. 8. PSD of streamwise velocity fluctuations (u') for the current-only and four wave cases simulated with the frequency normalized by the rotational frequency of the turbine (f_T).

B. Time-averaged wake dynamics over the vertical center plane

The normalized time-averaged streamwise velocity (U/U_0) developed around the simulated tidal turbine for the current-only and wave cases are presented in Fig. 9. In the case without waves, there is a high velocity region above the turbine due to vertical blockage as there is a relatively small clearance between turbine top-tip height and mean water level. Behind the turbine, a low-velocity wake region is developed which, eventually, recovers its momentum further downstream. The prediction of the mean hydrodynamic coefficients, time-averaged velocity field, and turbulence intensity at $x/D = 4$ and 8 in the wake downstream of a two-row array for the same turbine setup was validated in Ouro *et al.* [37], albeit the free surface was modelled as a rigid-lid and no waves were included.

The presence of waves changes the near-wake streamwise velocity (U/U_0) pattern in the upper wake region, as the transport and coherence of the tip vortices are affected, as shown in the previous section. For the shortest wave ($kh = 2.827$), there is an intermittent distribution of velocity maxima and relatively lower values between the turbine top-tip height and free surface with a near-wake behind the turbine that features a higher streamwise velocity than in the current only case. A somewhat similar distribution of U/U_0 is observed for the case with $kh = 0.978$ but with larger velocity values in the region after $x/D \geqslant 3$. As wavelength increases, the velocity recovery at the vertical plane across the turbine center seems to increase although its distribution for $kh \geqslant 0.707$ seems similar. For the shallowest surface wave, $kh = 0.353$, the flow over the turbine rotor location also shows increased velocity values but up to $x/D \approx 2$ when in the other cases this extends to further downstream.

Turbine- and wave-induced changes to the time-averaged normalized vertical velocity field are shown in Fig. 10 over the vertical plane at the turbine's center. In the no-wave case only a negative velocity region is seen behind the turbine as there is an entrainment from the upper region (elevation of highest velocities, as the approach flow has a shear distribution [69] and bypass flow is higher) into the wake region. Surface waves disturb the mean vertical velocity field in both near- and far-wake regions. LES results from the shortest wavelength ($kh = 2.827$) show intermittent positive and negative values in the downstream projection of the top-tip height until about $x/D = 7$–8, a consequence of the upwards and downwards motion of tip vortices due to wave action. At hub height, the negative vertical velocity region features larger velocity magnitude than in the no-wave case. The far-wake for this nearly deep-water wave case is characterized by positive
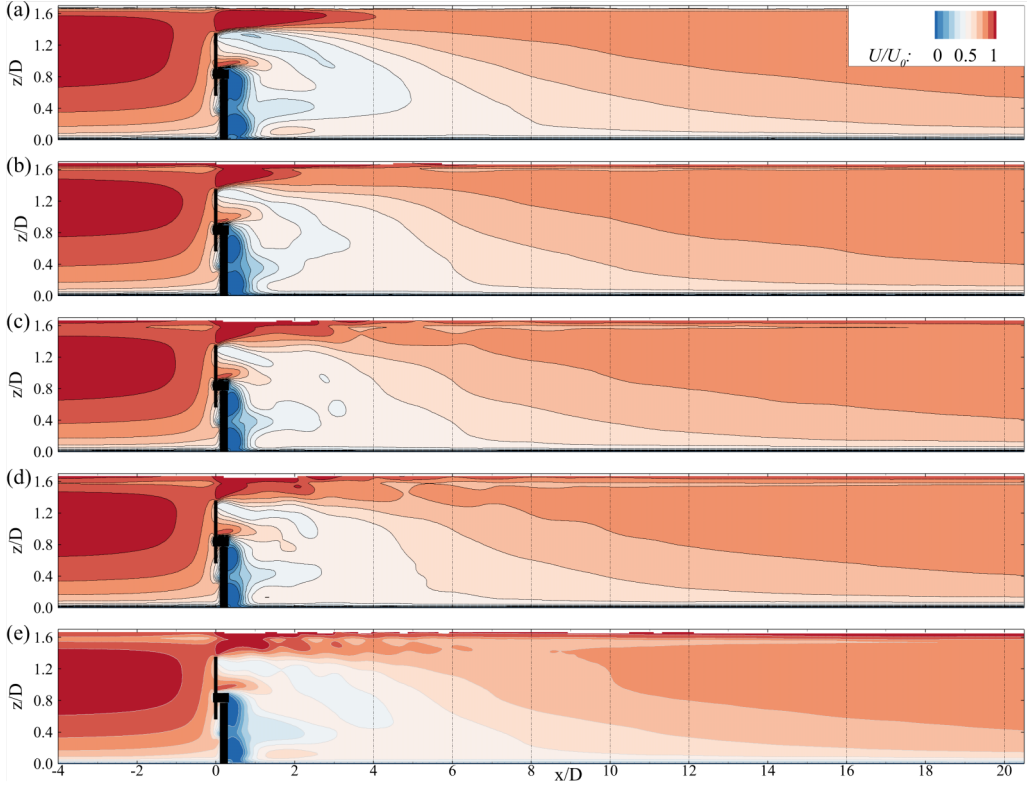
FIG. 9. Contours of normalized streamwise velocity (U/U_0) over a xz plane at $y/D = 0$. Results from the (a) no wave, (b) $kh = 0.353$, (c) $kh = 0.707$, (d) $kh = 0.978$, and (e) $kh = 2.827$.

vertical velocities of larger magnitude than any of the other wave cases. In a later section through the mean kinetic energy budget analysis, it is shown that this positive vertical velocity results from the higher lateral bypass flow.

For the cases with intermediate to shallow wave conditions, the near-wake region of large negative W/U_0 values becomes less coherent in space and extends for a shorter downstream distance, e.g., comparing that for $kh = 0.353$ to 0.978. Conversely, the positive vertical velocity region in the far wake reduces in magnitude with increasing wavelength, and the $kh = 0.353$ is similar to the current-only results.

Contours of velocity fluctuation intensity are presented in Figs. 11 and 12 (and in the Appendix for v' in Fig. 20), highlighting a larger impact of the waves over the streamwise vertical plane across the turbine center. Note that in absence of waves, these velocity fluctuation intensities are analogous of turbulence intensity, whereas when waves are present they comprise both a periodic nonturbulent fluctuation and turbulence, hence denoted herein as the velocity fluctuation intensity normalized to the time-averaged velocity fluctuation. In the absence of waves, there are two regions of high streamwise turbulence intensity (u') corresponding to the tip vortices and wake of the supporting structure. The shortest wavelength [$kh = 2.827$, Fig. 11(e)] waves introduce fluctuations mostly at the upper layer of the water column, although it extends down through midwater depth, whereas if truly deep water, $kh \geqslant \pi$, there would be no change below mid-depth. In the top tip vortex region, up to $x/D = 4$, there are pockets of high mean streamwise velocity fluctuation, whose spacing is of approximately $1D$, i.e., $0.27\lambda_w$.

Figure 11(c) presents the time-averaged streamwise velocity fluctuation intensity u'/U_0 for the $kh = 0.978$ case, with a global increase in fluctuation intensity across the water column. Its
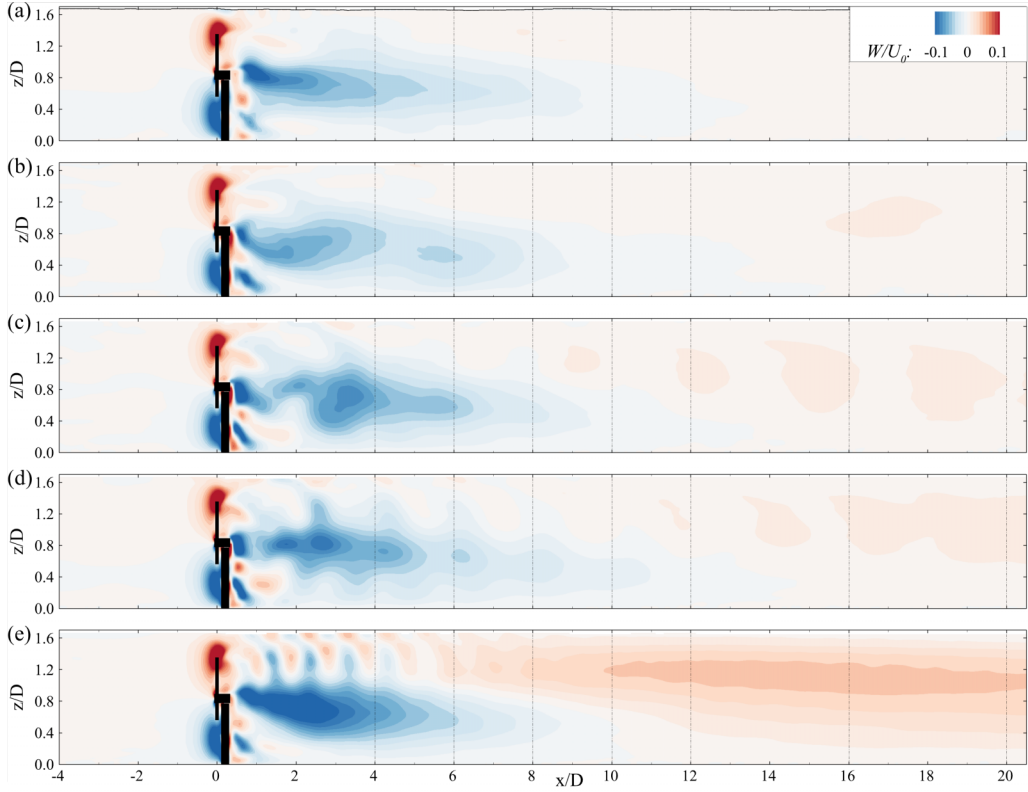
FIG. 10. Contours of normalized vertical velocity (W/U_0) over a xz plane at the $y/D = 0$. Results from the (a) no wave, (b) $kh = 0.353$, (c) $kh = 0.707$, (d) $kh = 0.978$, and (e) $kh = 2.827$.

distribution in the near-wake notably differs to that in the current-only and short-wave cases, with higher intensity levels. The intermittent pattern of high u' regions, especially near the free surface, again denote the signature of the periodic transport of top tip vortices due to wave action, already revealed in the spatial-correlation contours in Fig. 7. The distance between regions of high u'/U_0 is of approximately $2D$ or $0.18\lambda_w$ for this wave case. Increasing wavelengths in cases with $kh = 0.707$ and 0.353, exhibit a larger wave action deeper in the water column, with the alternate areas of high u'/U_0 at larger streamwise distances approximately $3D$ ($0.20 \lambda_w$) and $6D$ ($0.20 \lambda_w$) for the $kh = 0.707$ and 0.353 cases, respectively. For all these intermediate cases the separation between regions of consecutive low (or high) turbulence intensity approaches $0.20 \lambda_w$. In addition, for the longest wavelength, these regions of mean streamwise velocity fluctuation also appear to be distributed in an oblique pattern at about $45°$. Considering the mean convection time for the wake intermittency due to waves, it can be obtained as the separation between regions of high and low turbulence intensity and the wave period, yielding relative velocities (U/U_0) of 0.72, 0.97, 1.03, and 1.08 for kh of 2.827, 0.978, 0.707, and 0.353, respectively.

The mean vertical velocity fluctuation intensity field (w'/U_0) for the cases simulated presented in Fig. 12 reveals again the region of the turbine wake affected by the waves. In the no-wave case, the top tip vortices advected downstream result in large w'/U_0 values, principally over the region to $x/D \leqslant 3$. For the shortest wavelength, $kh = 2.827$, the wake behind the turbine's support structure appears unaffected by waves, while the near free-surface region exhibits high levels of w'/U_0 with a nearly constant intermittency of high and low values. In the intermediate cases ($kh = 0.978$ and 0.707), the magnitude of w'/U_0 near the free surface diminishes and the patchiness
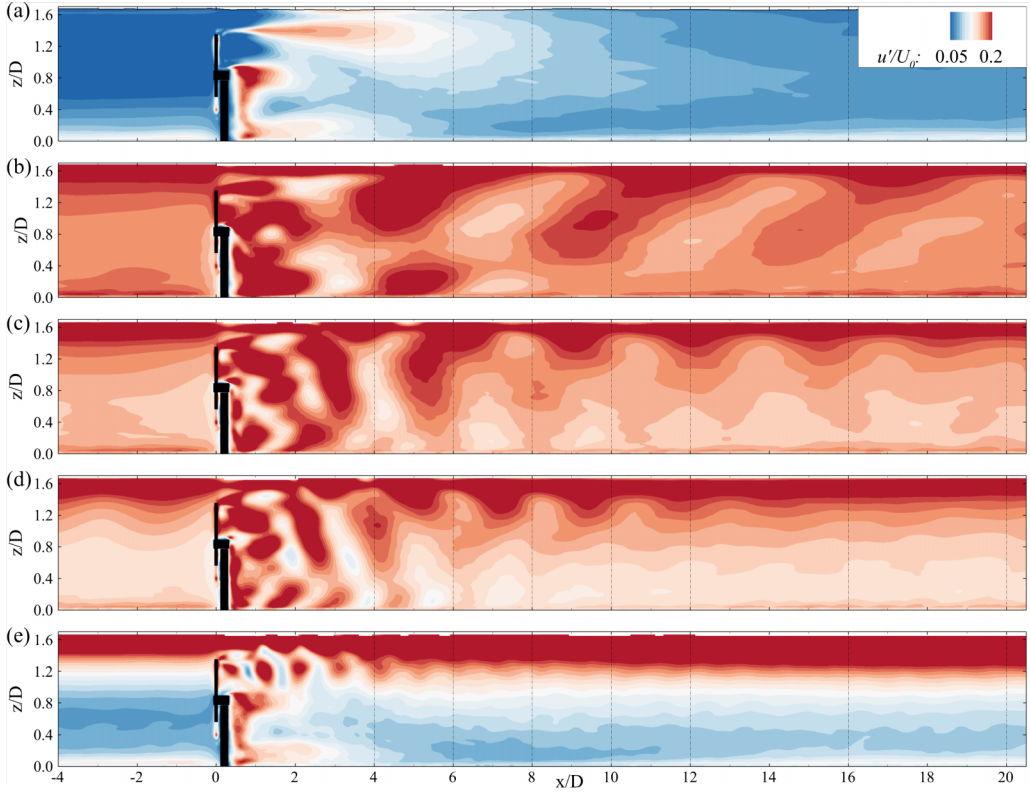
FIG. 11. Contours of streamwise velocity fluctuation intensity (u'/U_0) over a xz plane at the $y/D = 0$. Results from the (a) no wave, (b) $kh = 0.353$, (c) $kh = 0.707$, (d) $kh = 0.978$, and (e) $kh = 2.827$.

of the distribution of pockets of high w'/U_0 are more clearly defined with an increasing spacing as wavelength increases. The distribution of w'/U_0 across the vertical plane at the turbine center resembles that of the no-wave case, namely the top tip vortex signature is observed with the support structure's wake also present but with higher values. In the region of $x/D = 4$–6 there is an increase in w'/U_0 that is not observed in the current-only case.

In the wake recovery behind a tidal stream turbine, the correlation between streamwise and vertical velocity fluctuations ($u'w'$, i.e., corresponding to the vertical Reynolds stress when excluding waves) is essential to understand the mixing between the turbine's wake and ambient flow. The contours of $u'w'/U_0^2$ are presented in Fig. 13 at the center of the turbine's location over a vertical xz plane. In the current-only case there is a region of negative values at top tip height up to $x/D \approx 6$, denoting downwards motion of momentum fluctuations, while below the bottom tip there is a region of upwards motion.

Surface waves induce an upwards and downwards motion on the top tip vortex location which modify the vertical fluctuation of momentum exchange in the upper layer of the water column, as shown in Figs. 2 and 3. For the $kh = 0.707$ case [Fig. 13(c)], the regions of negative and positive $u'w'$ appear to be distributed at an angle of $30°$ with the vertical direction, not evident from the previous flow quantities. The latter pattern is similar to that found in the longest wave case but at a larger angle of approximately $45°$ with the vertical direction as seen in the u'/U_0 contours [Fig. 11(b)]. Conversely, for the shortest wavelength, the alternate distribution of downwards and upwards fluctuating momentum transfer is seen to be distributed in fairly uniform regions in the streamwise direction with a wavelength of approximately $D/2$ [Fig. 13(e)]. In the far-wake region
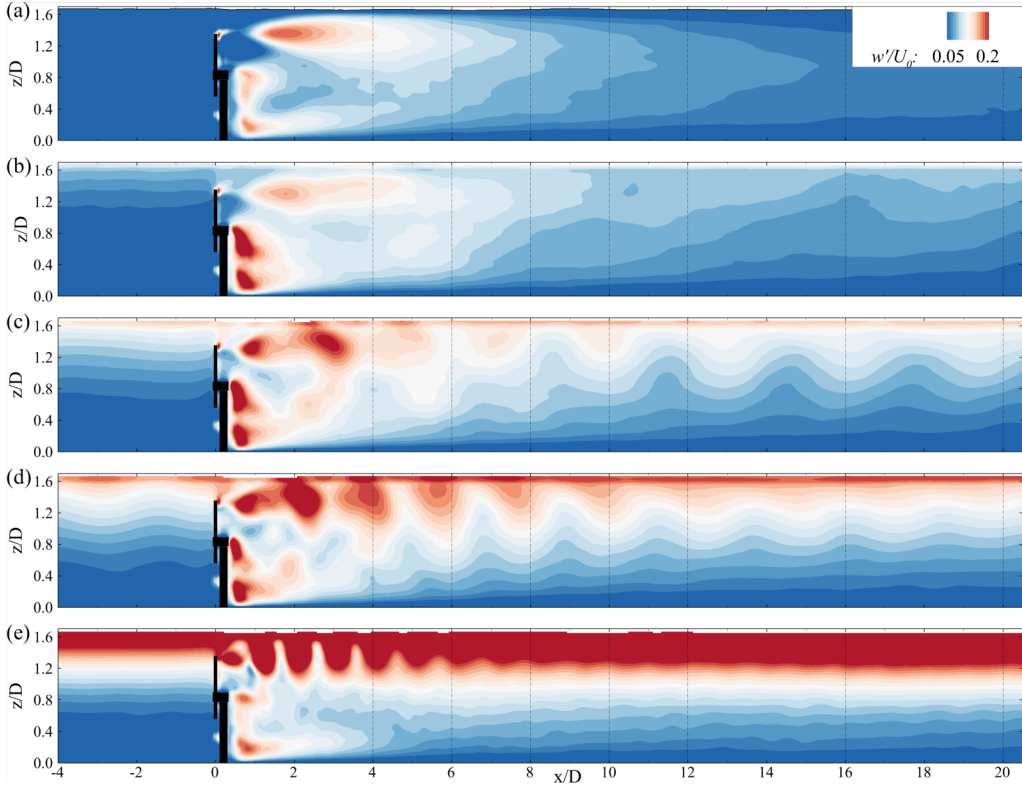
FIG. 12. Contours of vertical velocity fluctuation intensity (w'/U_0) over a xz plane at the $y/D = 0$. Results from the (a) no wave, (b) $kh = 0.353$, (c) $kh = 0.707$, (d) $kh = 0.978$, and (e) $kh = 2.827$.

after $x/D = 8$, a downwards momentum exchange near the free surface is observed unlike in the other wave cases. For the intermediate wavelengths, there is a larger contribution of negative $u'w'$ in the upper water column region, behind the turbine, until a downstream distance of approximately $8D$ [Fig. 13(d)].

To further explain the discontinuous streamwise evolution in the unsteady flow quantities, the contours of the horizontal unsteady momentum exchange ($u'v'$, i.e., horizontal Reynolds stress when no waves are present) is presented in Fig. 14 over a horizontal plane at hub height. Compared to the current-only case in which the shear layers are clearly identifiable at each edges of the horizontal wake region, the wave cases show an intermittent distribution. Figures 14(b) to 14(e) show that the distance between hot spots of $u'v'/U_0^2$ increase with wavelength, which remains relatively uniform up to a distance of about $x/D = 24$. For longest wavelength case, $kh = 0.353$, the large regions of positive and negative horizontal momentum exchange are at the same downstream locations, while for the other intermediate but shorter waves cases ($kh = 0.978$ and 0.707) these are alternated.

The time-averaged quantities show a distinct distribution such as regularly distributed regions of low and high velocity fluctuations, which may be linked to actual turbine operating point (determined by the turbine rotational speed and onset mean velocity), wave period, and amplitude, current and wave directions and relative turbine submergence. For scenarios with turbines operating at slower or faster rotational speeds slight differences in the wake pattern could be observed, which will be the scope of future work.
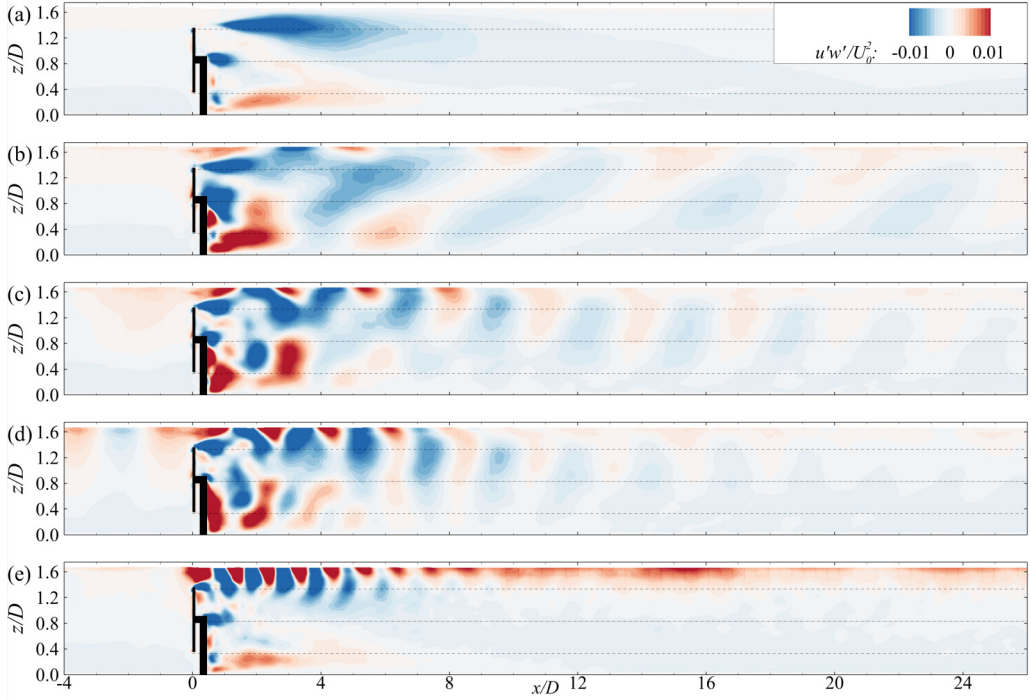
FIG. 13. Contours of normalized vertical Reynolds shear stress ($u'w'/U_0^2$) over a xz plane at the $y/D = 0$. Results from the (a) no wave, (b) $kh = 0.353$, (c) $kh = 0.707$, (d) $kh = 0.978$, and (e) $kh = 2.827$.

C. Wake recovery and mean kinetic energy budget

As the flow field downstream of the tidal stream turbine notably differs under the action of surface waves, it is essential to quantify the downstream momentum recovery in view of deploying further rows of turbines. Thus, the evolution of the disk-averaged velocity deficit $[\Delta U = U(x) - U_0]$ downstream of the turbine is presented in Fig. 15 with the streamwise variation of the disk-averaged velocity deficit for the current-only and wave cases. In the presence of waves, the rate of wake recovery is increased (the recovery distance reduces) but at different rates depending on the wave characteristics. For the largest wave number considered, $kh = 2.827$, the wake recovery is slightly faster than for the current-only case. Compared to the other wave cases, the $kh = 2.827$ case has the largest ΔU up to a distance of $x/D = 12$–14. After this point its velocity deficit becomes the smallest among all of the wave cases. Results for the intermediate and nearly shallow waves show an almost identical wake recovery throughout the wake length, faster than the nearly deep-water wave in the near- and midwake regions, i.e., $x/D \leqslant 12$.

To understand the driving component to the faster wake recovery in the wave cases than in the current-only simulation, the budget of the mean kinetic energy (MKE) (MKE $= 0.5\bar{U}_i^2$, with $i = 1, 2, 3$) is analyzed, which assuming steady-state conditions [33,71,72], reads:

$$0 = \underbrace{\langle u_j \rangle \frac{\partial}{\partial x_j}\left(\frac{1}{2}U^2\right)}_{C_i} \underbrace{-U\frac{1}{\rho}\frac{\partial P}{\partial x_i}}_{PT} + \underbrace{\frac{\partial}{\partial x_j}\left[(\nu + \nu_t)\frac{\partial}{\partial x_j}\left(\frac{1}{2}U^2\right)\right]}_{VT} \underbrace{-(\nu + \nu_t)\left(\frac{\partial U}{\partial x_j}\right)^2}_{Diss}$$

$$\underbrace{-\frac{\partial}{\partial x_j}(U\langle u'_i u'_j\rangle)}_{TT_i} + \underbrace{\langle u'_i u'_j\rangle\frac{\partial U}{\partial x_j}}_{TP_i},\tag{14}$$
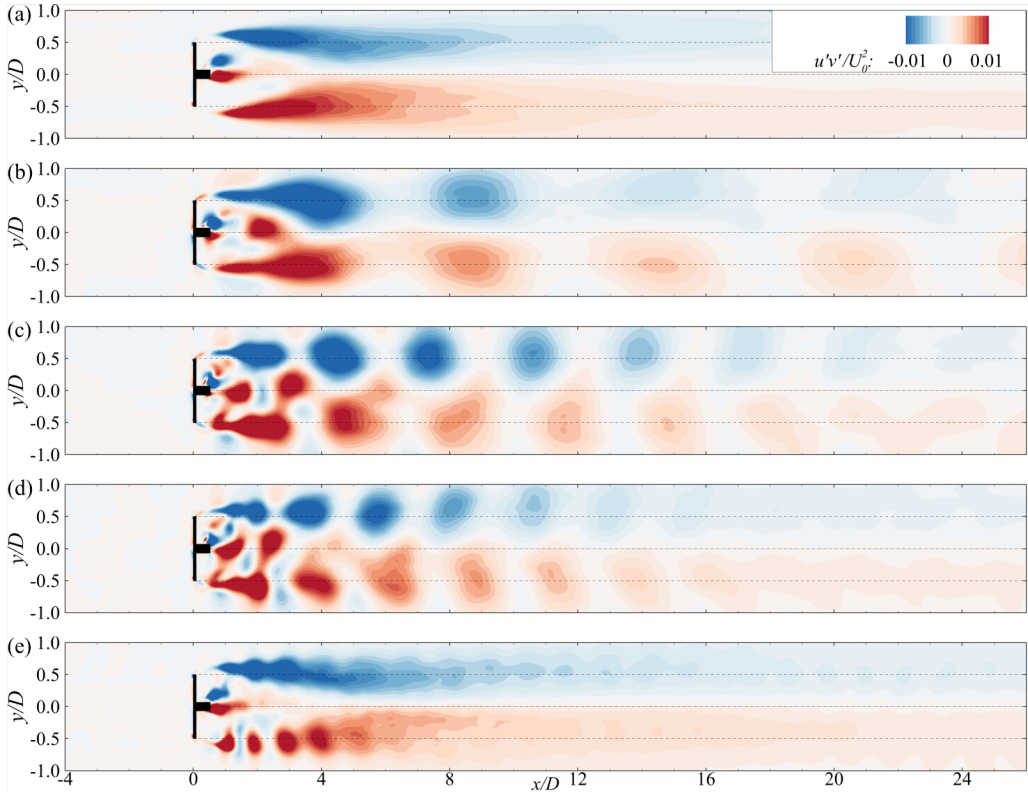
FIG. 14. Contours of normalized transverse Reynolds shear stress ($u'v'/U_0^2$) over a xy plane at hub height. Results from the (a) no wave, (b) $kh = 0.353$, (c) $kh = 0.707$, (d) $kh = 0.978$, and (e) $kh = 2.827$.
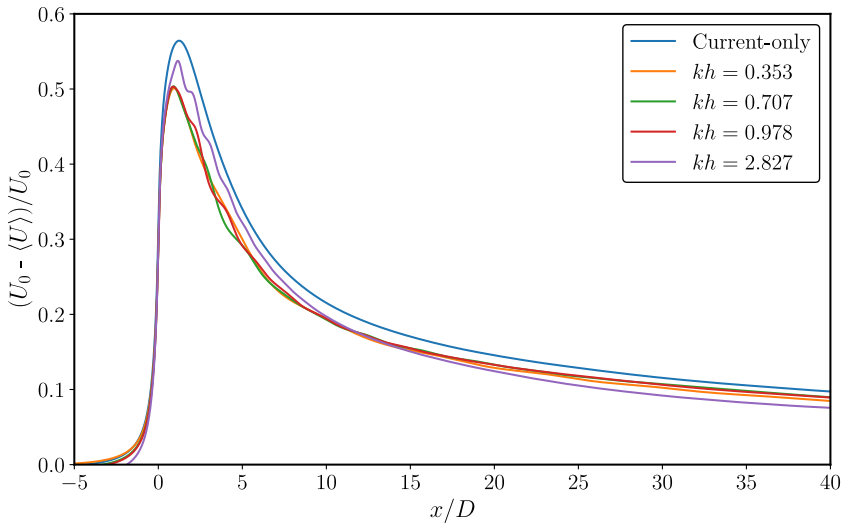

FIG. 15. Streamwise evolution of disk-averaged velocity deficit ($(U_0 - \langle U \rangle)/U_0$) for the current-only and wave-current simulations.
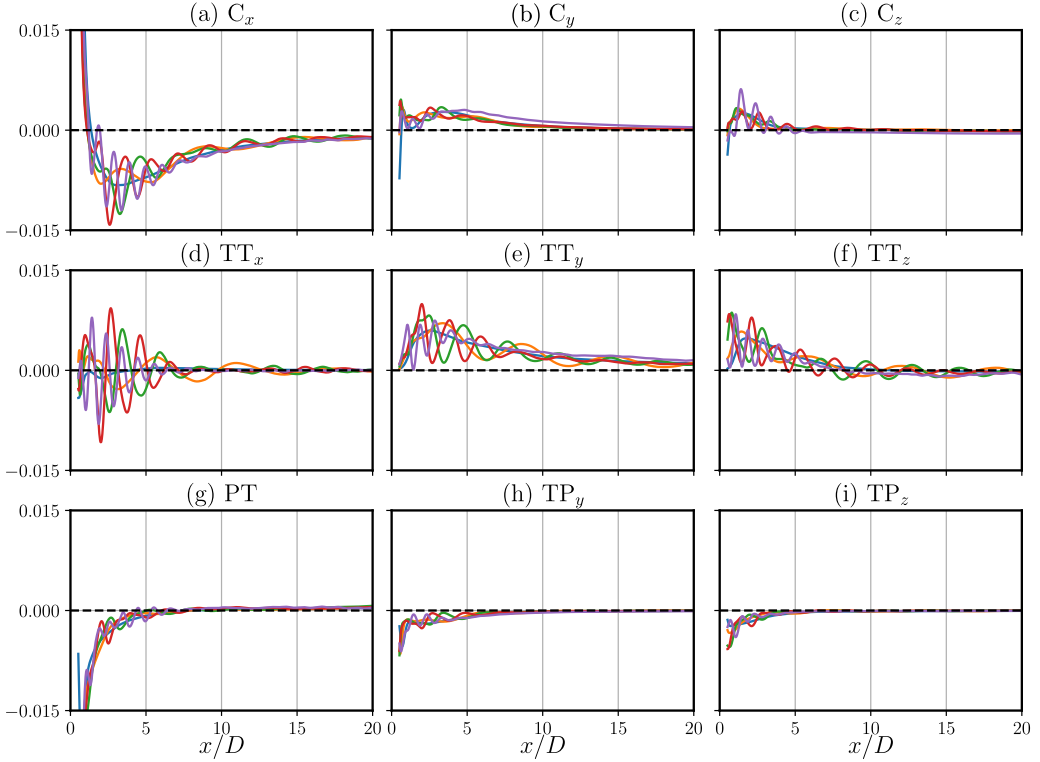
FIG. 16. Streamwise evolution of mean kinetic energy budget [Eq. (14)] terms for the current-only case and wave-current simulations. Legend of simulated cases as in Fig. 15.

where P denotes time-averaged pressure field and ν_t is the mean viscosity added by the subgrid scale model. The meaning of the various terms in this balance equation for the mean kinetic energy is as follows: C_i is the convection of the mean kinetic energy by the mean flow; PT is the mechanical work produced by gradients in the mean pressure field that transports MKE; VT is the work done by the viscous stresses; Diss is the viscous dissipation of MKE; TT_i is the transport done by the turbulence stresses, representing the transport by Reynolds stresses; and TP_i is the work of deformation by turbulence stresses which represents the destruction of MKE turned into turbulent kinetic energy production.

These terms of Eq. (14) are integrated across the rotor region, i.e., $-1/2 \leqslant y/D \leqslant 1/2$ and $-1/2 \leqslant z/D \leqslant 1/2$ to evaluate their relevance in wake recovery. The downstream distribution of the main terms in the MKE budget behind the turbine presented in Fig. 16, excluding terms such as viscous dissipation whose contribution is negligible. The surface waves lead to a sinusoidal spatial variation of the terms (even if these are time-averaged) in the near-wake field due to different modulation of the transport of tip vortices by the wave. The wavelength of this spatial variation is nearly half of the wavelength. This is most noticeable in the MKE transport by turbulent stresses (TT_i), which follows the distribution of flow field variables shown in contours plots of Figs. 9–14. The no-wave case shows a smoother behavior that resembles a low-pass filter for some of the MKE equation terms. The streamwise component of the MKE convection contributed negatively to the MKE, i.e., induces a delay in MKE, while the transverse and vertical aid to gain MKE albeit with lower magnitude. The transverse turbulent transport terms (TT_y) contributes to the replenishment of MKE over the wake length. The vertical component term (TT_z) also provides a gain of MKE up to $x/D = 8$–10, location at which it has a negligible magnitude for the current-only case and

it alternates between gain and loss of MKE in the downstream direction for the wave cases. In its streamwise component (TT_x), the transport due to velocity fluctuations shown in Fig. 16(d) presents large differences between the no-wave (with a reduced contribution to the MKE budget) and wave cases. For the latter, a varying contribution to delay (negative value) and replenishment (positive value) is seen with a sinusoidal shape whose wavelength agrees with that seen in the time-averaged streamwise velocity fluctuation (Fig. 11). The net contribution is, however, negligible as shown later. The spatial undulations in the downstream direction seen in the previous terms are mostly damped in the pressure transport term [Fig. 16(g)] for the longest wavelengths, e.g., $kh = 0.353$. Production of turbulent kinetic energy terms exhibit a relatively low contribution, as does the viscous dissipation which is not plotted for convenience.

The net contribution of the MKE terms to the wake recovery is further analyzed with their integration in the downstream direction. First, these are integrated between $0.5 \leqslant x/D \leqslant 12$, as that up to $x/D = 12$ the shortest wave case ($kh = 2.827$) has the largest disk-averaged velocity deficit compared to the other wave cases, shown in Fig. 15. Then, the region between $12 \leqslant x/D \leqslant 20$ is analyzed as now the shortest wave case achieves the fastest wake recovery rate. Results are presented in Fig. 17 including all the terms from the MKE budget [Eq. (14)]. In the region $x/D \leqslant 12$, terms corresponding to the MKE convection C_y and C_z and turbulent transport TT_y and TT_z have a positive net contribution and responsible to aid the replenishment of MKE in the wake. Conversely, the streamwise MKE convection C_x, pressure term PT and turbulence production terms TP_y and TP_z infer a delay in the MKE recovery. After $x/D \geqslant 12$, the transverse contribution to the MKE convection C_y and turbulent transport TT_y continue to be the main sources of MKE replenishment with the pressure term PT now also adding to this. They are balanced with the negative contribution to MKE budget mainly from the streamwise MKE convection C_x and at a lower extent from the vertical components of convection C_z and turbulent transport TT_z.

When comparing the integrated values across different wave conditions, in the first region up to $x/D \leqslant 12$ the distribution is quantitatively similar between cases. Results from the current-only case and longest wave are quite similar in magnitude while the shortest wavelength features larger values in the contribution from the transverse convection term C_y while smaller from its vertical component TT_z. However, after $x/D \geqslant 12$, the shortest wavelength ($kh = 2.827$) exhibits a larger contribution from most of the terms, mainly C_y, C_z, TT_y, and TT_z as seen in Fig. 16, while the pressure term PT and C_x are similar to the other wave case and current only simulation. Along this wake region, the transverse terms C_y and TT_y are those principally aiding the MKE recovery while their vertical counterparts C_z and TT_z work to delay it together with C_x. At this distance downstream of the turbine, the mixing of tip vortices with the ambient flow is reduced as these flow structure already lose coherence a few diameters downstream of the device, thus their net contribution to the MKE budget after $x/D \geqslant 12$ is negligible.

V. HYDRODYNAMIC FORCES ON THE TURBINE

The time-averaged hydrodynamic thrust ($\overline{C_T}$) and power ($\overline{C_P}$) coefficients for the simulated cases and those from the experiments from Stallard *et al.* [69], to be compared with the current-only predictions as waves were not included, are presented in Table II. Values predicted from the current LES-ALM for the current-only are in good agreement with the experiments, with a very similar thrust coefficient and slightly overestimated power coefficient. When waves are introduced, both turbine performance and thrust varies. For the shortest wave, both coefficients increased with a notable 6% higher power coefficient. Conversely, for the simulations with intermediate waves these coefficients decrease with increasing wavelength, especially for the longest wave ($kh = 0.353$) in which $\overline{C_P}$ reduces 14% compared to the current-only case. Note that the simulations considered a turbine rotating a fixed rotational speed (different to reference experiments from Stallard *et al.* [69] which were run at a constant torque), thus the operating point (tip-speed ratio) varies in time depending on the onset flow conditions, e.g., with higher tip-speed ratio during periods of wave troughs and alternatively at lower tip-speed ratio during wave crests.
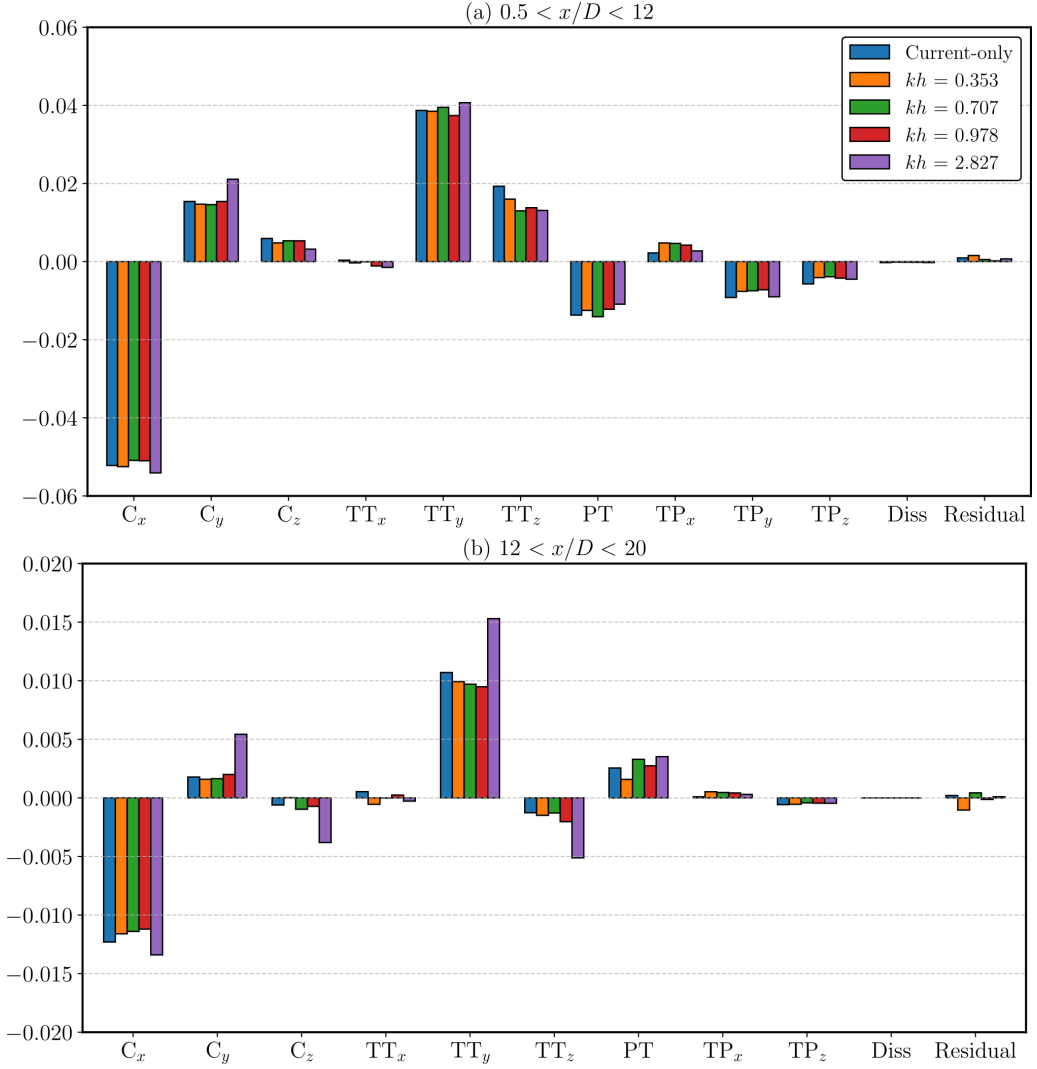
FIG. 17. Integrated values of the MKE budget terms [Eq. (14)] over the downstream wake between (a) $0.5 \leqslant x/D \leqslant 12$ and (b) $12 \leqslant x/D \leqslant 20$ for the current-only and wave cases simulated.

TABLE II. Hydrodynamic coefficients of mean thrust ($\overline{C_T}$) and power ($\overline{C_P}$) for the different cases simulated.

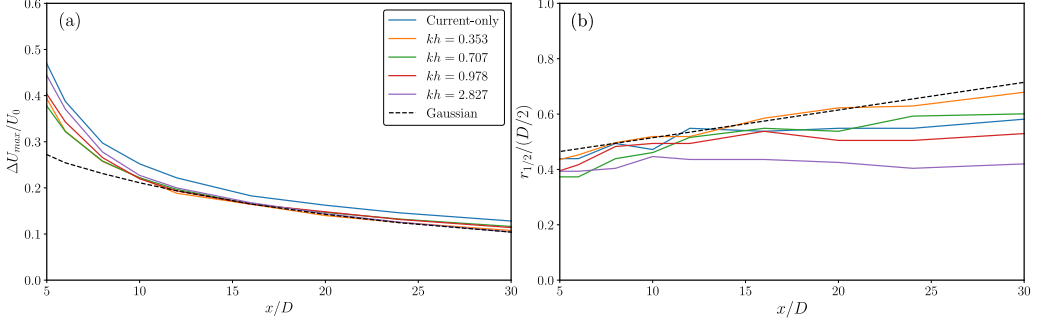| Case	$\overline{C_T}$	$\overline{C_P}$
Experiments [69] (current-only)	0.816	0.274
Current-only	0.822	0.305
$kh = 0.353$	0.781	0.262
$kh = 0.707$	0.801	0.283
$kh = 0.978$	0.810	0.292
$kh = 2.827$	0.848	0.323

FIG. 18. Streamwise evolution of normalized (a) maximum velocity deficit $\Delta U_{\max}/U_0$ [Eq. (16)] and (b) wake half-width $r_{1/2}/(D/2)$ [Eq. (17)] for the current-only and wave-current simulations, where constants of $k^* = 0.25$ TI and $\varepsilon = 0.32 \, \beta^{0.5}$ are used.

VI. SEMIEMPIRICAL GAUSSIAN WAKE MODEL FOR TIDAL TURBINES IN PRESENCE OF WAVES

Representing the time-averaged velocity field in the turbine wake region can inform the development of low-order engineering models [73,74]. These are commonly based on the assumption of a Gaussian velocity profile in the radial direction [$g(r)$, with $r^2 = y^2 + z^2$ considering y and z the transverse and vertical coordinates centered at the turbine rotor] together with a given velocity scale [$C(x)$] that evolves in the streamwise direction downstream of the turbine. In channels of shallow depth to diameter, recovery of the far-wake that may be considered symmetric about y direction. The normalized velocity deficit [$\Delta U(x, r)/U_0$] is then determined as

$$\frac{\Delta U(x, r)}{U_0} = C(x) \times g(r) = \frac{\Delta U_{\max}}{U_0}(x) \times \exp\left(-\frac{r^2}{2 \, r_{1/2}^2}\right). \tag{15}$$

The velocity scale and wake shape are characterized over the wake length, taking transverse profiles of the normalized velocity deficit [$\Delta U(x, r)U_0$] expanding D to each side of the wake at hub height over various stations downstream of the turbine. The velocity scale is obtained from the maximum velocity deficit of each downstream transverse profile, with results provided in Fig. 18(a) in a semilog scale for the simulated cases. The transverse half-width ($r_{1/2}$) is obtained as the lateral position at which the velocity deficit is half the maximum value. Considering a semiempirical Gaussian wake model [69,73], this reads:

$$\Delta U_{\max} = 1 - \sqrt{1 - \frac{C_T}{8(r_{1/2}/D)^2}}, \tag{16}$$

$$\frac{r_{1/2}}{D/2} = k^* \frac{x}{D} + \varepsilon. \tag{17}$$

The model proposed by Bashtankhah and Porté-Ágel [73] for wind turbine wakes is modified to provide a better prediction of the tidal turbine wake in presence of waves. This is necessary as the velocity deficit shortly downstream of the turbine differs. Thus, the Gaussian wake model is modified to adopt the following wake expansion rate (k^*) and initial wake width (ε), as:

$$k^* = 0.25 \cdot \text{TI}, \tag{18}$$

$$\varepsilon = 0.32 \cdot \beta^{0.5}. \tag{19}$$

Here $\beta = (1 + \sqrt{1 - C_T}/\sqrt{1 - C_T})/2$. Note that the value of the initial wake width is larger than that in wind turbines, equal to $\varepsilon = [0.2 - 0.25] \cdot \beta^{0.5}$, indicating that there is a higher velocity deficit
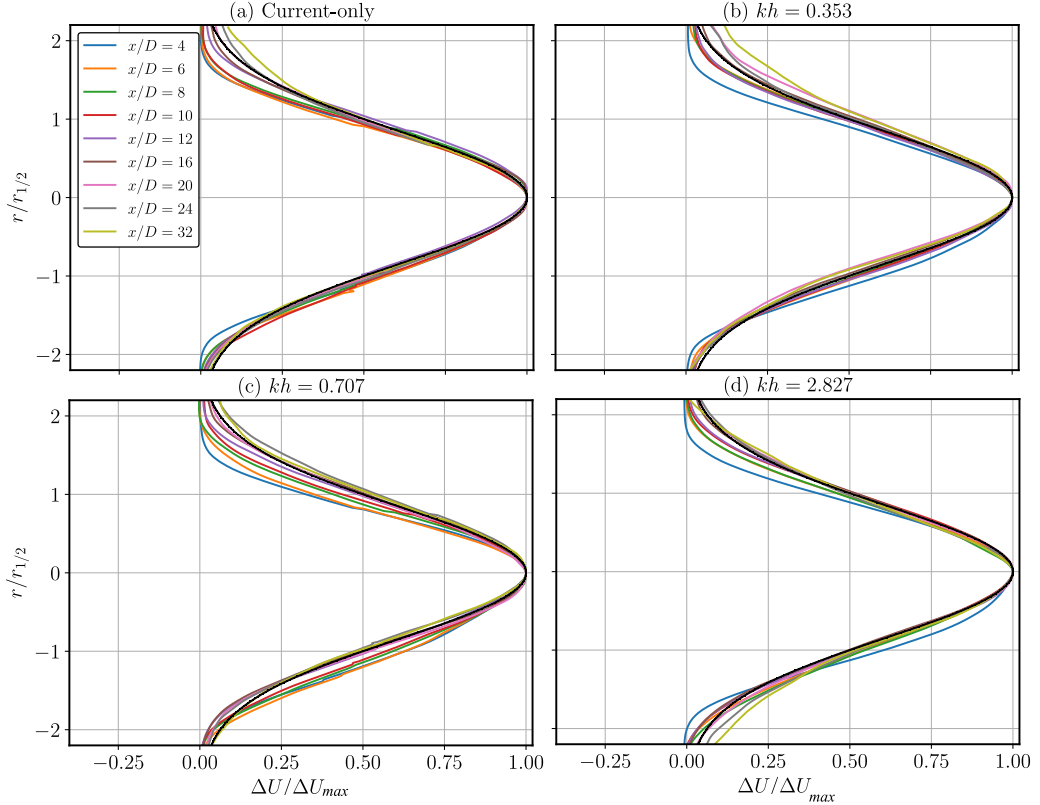
FIG. 19. Self-similar normalized velocity deficit ($\Delta U / \Delta U_{\max}$) transverse profiles with coordinates normalized by the wake width $r_{1/2}$ at various downstream locations from the (a) current-only, (b) $kh = 0.353$, (c) $kh = 0.707$, and (d) $kh = 2.827$ simulations. Gaussian shape indicated by the black solid line.

(i.e., lower velocities) immediately downstream of the tidal turbine, owed to the large sectional blockage unlike wind turbines that operate in a less constrained (atmospheric) environment.

For the present cases, the onset turbulence intensity over the rotor plane area excluding the action of the waves is approximately 4%. Waves modulate the magnitude of the wake velocity, as seen at $x/D = 4$, in which the no-wave case features the largest velocity deficit that is slightly reduced in the shortest wave case ($kh = 2.827$). In the simulations with longer waves, the velocity deficit at this location ($x/D = 4$) is reduced to a similar value of $\Delta U_{\max}/U_0$ approximately 0.45. In the intermediate wake region, between $x/D = 4$–12, $\Delta U_{\max}$ recovers at different rates for all wave cases to reach the same maximum velocity deficit value at $x/D \approx 12$, after which $\Delta U_{\max}$ decays proportional to $(x/D)^{-1/2}$ as expected for an axisymmetric wake [69]. For the current-only case, the velocity deficit is consistently larger than in the wave cases, in agreement with the disk-averaged wake velocity shown in Fig. 15.

The suitability of using a Gaussian wake model for the semiempirical representation of turbine wakes is assessed in Fig. 19 with comparisons of the normalized velocity deficit distribution ($\Delta U / \Delta U_{\max}$) over the normalized transverse direction ($r/r_{1/2}$) obtained at downstream stations for the no-wave case and three wave cases ($kh = 0.353$, 0.707, and 2.827). When normalizing the velocity magnitude in the wake region by the maximum velocity deficit, the profiles follow the Gaussian wake model for all cases irrespective of the wave-current conditions. At $x/D = 4$ the velocity profile is narrower than that predicted by the Gaussian wake model. After $20D$ downstream, largest half-width wake spread is seen for the longest wavelength case (smallest kh) while the

half-width of the shortest wavelength (largest kh) is most similar to current-only case. These results show that semiempirical wake models are valid to be applied to tidal turbine wakes even in presence of waves, with updated recovery rates [or constants of Eqs. (18) and (19)] that may be expected to differ with amplitude as well as with kh.

VII. CONCLUSIONS

This paper presents the results of high-fidelity large-eddy simulations of a tidal stream turbine operating in a turbulent open-channel flow with sheared onset velocity distribution to which four regular, following wave conditions of increasing wavelength are investigated. The wake developed behind the turbine is modulated by the wave-current conditions with notable differences between the nearly deep water wave case and the three intermediate waves. The instantaneous wake behavior is analyzed with contours of vorticity at different instants in time, which indicate that the tip vortices generated by the turbine blades near the free surface undergo a periodic, transient motion in the vertical direction during the wave cycle. During periods of increasing surface elevation (when moving from wave trough to crest), tip vortices are advected upwards due to the positive wave-induced vertical velocity, while the opposite is observed during the second half of the wave period. These unsteady onset conditions leads to intermittent vertical entrainment of tip vortices into the wake region, which leads to varying wake recovery distribution. The disk-averaged velocity for the intermediate wave cases is smallest up to a distance of 12 diameters (D) downstream of the turbine, while the nearly deep wave featured the fastest recovery rate from such distance and even up to $40D$. In all cases, the current-only conditions lead to the largest velocity deficit.

Quantification of the mean kinetic energy equation for the shortest wavelength shows that the main contributors to its replenishment are the transverse convection and turbulent transport, which are balanced by the analogous vertical terms and streamwise convection. The pressure transport term features a relatively minor role but contributing to a net loss of mean kinetic energy in the wake up to $12D$ downstream of the turbine while aiding in its replenishment in the region extending from $12 < x/D < 20$.

Analytical wake models are commonly used to represent the spatial evolution of the wake velocity deficit with simple formulas, e.g., a Gaussian shape for its radial distribution, which can yield a relatively good accuracy if the wake shape proves to be self-similar. Results from the wave-current conditions show that the turbine wake can be considered to have a Gaussian shape albeit its recovery rate is slightly increased compared to the current-only case. Transverse half-width is observed to be largest for the longest wavelength while for short waves the reduced transverse mixing leads to a narrower lateral distribution. Our results indicated that waves accelerate wake recovery for all wave-current cases.

Validation of the present simulations with experimental data that adopts following waves with shear turbulent currents is required to further elucidate the accuracy of the present results. Further work should analyze the changes in loading on the turbine due to the wave-current interaction, perturbations to the wave field due to the presence of a turbine and an array of turbines. These LES may also allow to refine turbine control including both regular and irregular waves.

The data that support the findings of this study are available from the corresponding author upon reasonable request.

APPENDIX

The mean transverse velocity fluctuation intensity (v'/U_0) is presented in Fig. 20. Since waves do not introduce a transverse component, v'/U_0 is dominated by the induced circulation due to the turbine's rotation and wake meandering. The distribution of v'/U_0 features a large similarity between the no-wave and wave cases, although here the peak magnitude is lower for all wave cases than in no-waves, perhaps indicating the more rapid streamwise breakdown of the tip-vortex helix (as observed in earlier figures). The top tip vortex region is observed to extend from $x/D = 1$ until 10 for the current-only case, while this reduces in streamwise extend and magnitude of v'/U_0 with increasing wavelength.
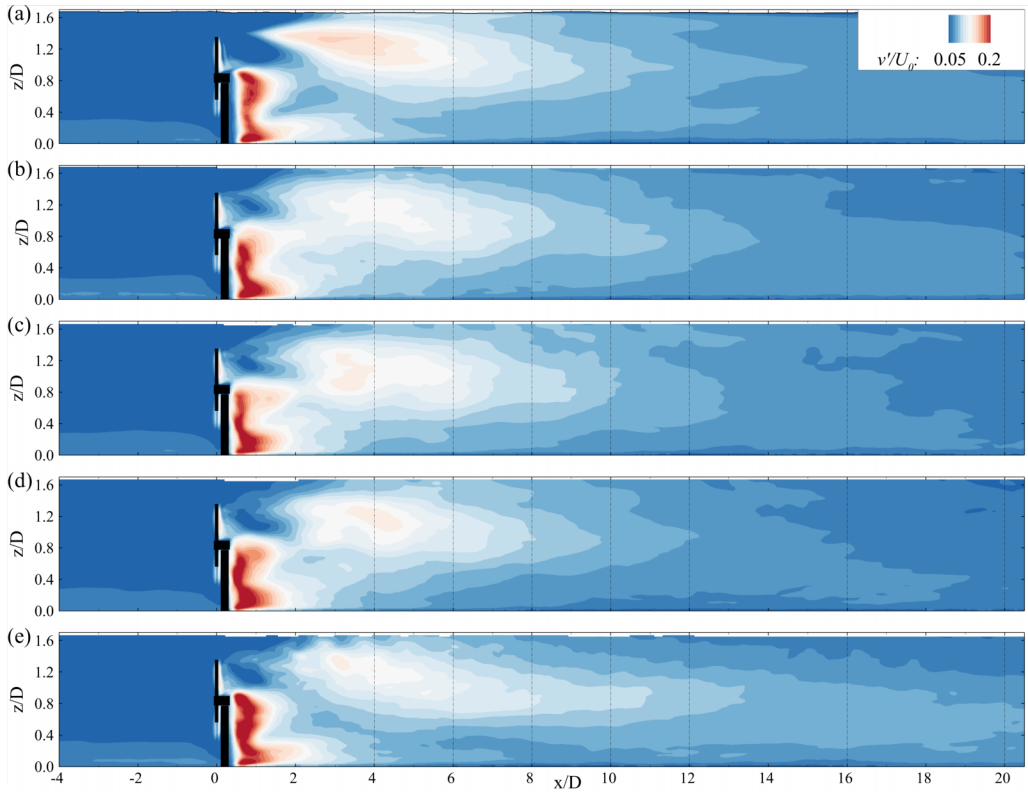

FIG. 20. Contours of transverse velocity fluctuation intensity (v'/U_0) over a xz plane at the $y/D = 0$. Results from the (a) no wave, (b) $kh = 0.353$, (c) $kh = 0.707$, (d) $kh = 0.978$, and (e) $kh = 2.827$.

[1] L. Perez, R. Cossu, A. Grinham, and I. Penesis, Seasonality of turbulence characteristics and wave-current interaction in two prospective tidal energy sites, Renew. Energy **178**, 1322 (2021).

[2] C. Peruzzi, D. Vettori, D. Poggi, P. Blondeaux, L. Ridolfi, and C. Manes, On the influence of colinear surface waves on turbulence in smooth-bed open-channel flows, J. Fluid Mech. **924**, A6 (2021).

[3] H. Mullings and T. Stallard, Analysis of tidal turbine blade loading due to blade scale flow, J. Fluids Struct. **114**, 103698 (2022).

[4] P. K. Stansby and P. Ouro, Modelling marine turbine arrays in tidal flows, J. Hydraul. Res. **60**, 187 (2022).

[5] C. Lloyd, M. Allmark, S. Ordonez-Sanchez, R. Martinez, C. Johnstone, G. Germain, B. Gaurier, A. Mason-Jones and T. O'Doherty, Validation of the dynamic load characteristics on a Tidal Stream Turbine when subjected to wave and current interaction, Ocean Eng. **222**, 108360 (2021).

[6] M. Togneri, I. Masters, and I. Fairley, Wave-turbulence separation at a tidal energy site with empirical orthogonal function analysis, Ocean Eng. **237**, 109523 (2021).

[7] M. Thiébaut, J. F. Filipot, C. Maisondieu, G. Damblans, R. Duarte, E. Droniou, N. Chaplain, and S. Guillou, A comprehensive assessment of turbulence at a tidal-stream energy site influenced by wind-generated ocean waves, Energy **191**, 116550 (2020).

[8] H. Mullings, S. Draycott, and T. Stallard, Turbine fatigue loadprediction from field measurements of waves and turbulence, in *Proceedings of the 15th European Wave and Tidal Energy Conference (EWTEC '23)* (Bilbao, Spain, 2023).

[9] N. Barltrop, K. Varyani, A. Grant, D. Clelland, and X. Pham, Wave-current interactions in marine current turbines, Proc. Inst. Mech. Eng., Part M **221**, 195 (2006).

[10] S. Draycott, G. Payne, J. Steynor, A. Nambiar, B. Sellar, and V. Venugopal, An experimental investigation into non-linear wave loading on horizontal axis tidal turbines, J. Fluids Struct. **84**, 199 (2019).

[11] T. de Jesus Henriques, S. Tedds, A. Botsari, G. Najafian, T. Hedges, C. Sutcliffe, I. Owen, and R. Poole, The effects of wave–current interaction on the performance of a model horizontal axis tidal turbine, Int. J. Mar. Energy **8**, 17 (2014).

[12] B. Gaurier, P. Davies, A. Deuff and G. Germain, Flume tank characterization of marine current turbine blade behaviour under current and wave loading, Renew. Energy **59**, 1 (2013).

[13] B. Gaurier, S. Ordonez-Sanchez, J.-V. Facq, G. Germain, C. Johnstone, R. Martinez, F. Salvatore, I. Santic, T. Davey, C. Old and B. Sellar, MaRINET2 tidal energy round robin tests—Performance comparison of a horizontal axis turbine subjected to combined wave and current conditions, J. Mar. Sci. Eng. **8**, 463 (2020).

[14] C. Faudot and O. G. Dahlhaug, Prediction of wave loads on tidal turbine blades, Energy Proc. **20**, 116 (2012).

[15] P. W. Galloway, L. E. Myers, and A. S. Bahaj, Quantifying wave and yaw effects on a scale tidal stream turbine, Renew. Energy **63**, 297 (2014).

[16] E. E. Lust, L. Luznik, K. A. Flack, J. M. Walker, and M. C. Van Benthem, The influence of surface gravity waves on marine current turbine performance, Int. J. Mar. Energy **3-4**, 27 (2013).

[17] L. Luznik, K. A. Flack, E. E. Lust, and K. Taylor, The effect of surface waves on the performance characteristics of a model tidal turbine, Renew. Energy **58**, 108 (2013).

[18] A. Nambiar, S. Draycott, G. S. Payne, B. Sellar, and A. Kiprakis, Influence of tidal turbine control on performance and loads, Appl. Ocean Res. **114**, 102806 (2021).

[19] S. Ordonez-Sanchez, M. Allmark, K. Porter, C. Lloyd, S. Ivan, T. O'Doherty and C. Johnstone, Analysis of a horizontal-axis tidal turbine performance in the presence of regular and irregular waves using two control strategies, Energies **12**, 367 (2019).

[20] R. Martinez, S. Ordonez-Sanchez, M. Allmark, C. Lloyd, T. O'Doherty, G. Germain, B. Gaurier and C. Johnstone, Analysis of the effects of control strategies and wave climates on the loading and performance of a laboratory scale horizontal axis tidal turbine, Ocean Eng. **212**, 107713 (2020).

[21] S. Draycott, J. Steynor, A. Nambiar, B. Sellar, and V. Venugopal, Experimental assessment of tidal turbine loading from irregular waves over a tidal cycle, J. Ocean Eng. Mar. Energy **5**, 173 (2019).

[22] S. Draycott, J. Steynor, A. Nambiar, B. Sellar, and V. Venugopal, Tidal turbine load variability in following and opposing irregular wave conditions, in *International Conference on Offshore Mechanics and Arctic Engineering* (American Society of Mechanical Engineers, 2020), Vol. 84416, p. V009T09A004.

[23] E. Fernandez-Rodriguez, T. Stallard, and P. Stansby, Experimental study of extreme thrust on a tidal stream rotor due to turbulent flow and with opposing waves, J. Fluids Struct. **51**, 354 (2014).

[24] S. Draycott, J. Steynor, A. Nambiar, B. Sellar, and V. Venugopal, Rotational sampling of waves by tidal turbine blades, Renew. Energy **162**, 2197 (2020).

[25] S. Draycott, A. Nambiar, B. Sellar, T. Davey, and V. Venugopal, Assessing extreme loads on a tidal turbine using focused wave groups in energetic currents, Renew. Energy **135**, 1013 (2019).

[26] T. Stallard, R. Collings, T. Feng, and J. Whelan, Interactions between tidal turbine wakes: Experimental study of a group of three-bladed rotors, Philos. Trans. R. Soc. A **371**, 20120159 (2013).

[27] Y. Zhang, W. Zang, J. Zheng, L. Cappietti, J. Zhang, Y. Zheng, and E. Fernandez-Rodriguez, The influence of waves propagating with the current on the wake of a tidal stream turbine, Appl. Energy **290**, 116729 (2021).

[28] W. Zang, Z. Yuquan, Z. Yuan, Z. Jisheng, G. Dawei, and E. Fernandez-Rodriguez, On the impact of waves and turbulence on the power fluctuations and wake structure of a tidal-stream turbine, Phys. Fluids **35**, 055115 (2023).

[29] S. C. Tatum, C. H. Frost, M. Allmark, D. M. O'Doherty, A. Mason-Jones, P. W. Prickett, R. I. Grosvenor, C. B. Byrne, and T. O'Doherty, Wave-current interaction effects on tidal stream turbine performance and loading characteristics, Int. J. Mar. Energy **14**, 161 (2016).

[30] S. Tatum, M. Allmark, C. Frost, D. O'Doherty, A. Mason-Jones, and T. O'Doherty, CFD modelling of a tidal stream turbine subjected to profiled flow and surface gravity waves, Int. J. Mar. Energy **15**, 156 (2016).

[31] D. Apsley, T. Stallard, and P. Stansby, Actuator Line CFD modelling of tidal-stream turbines, in *CORE2016—2nd International Conference on Offshore Renewable Energy* (2016).

[32] Z. Li, K. Ghia, Y. Li, Z. Fan, and L. Shen, Unsteady Reynolds-averaged Navier-Stokes investigation of free surface wave impact on tidal turbine wake, Proc. R. Soc. A **477**, 20200703 (2021).

[33] A. Posa and R. Broglia, Characterization of the turbulent wake of an axial-flow hydrokinetic turbine via large-eddy simulation, Comput. Fluids **216**, 104815 (2021).

[34] A. Posa and R. Broglia, Analysis of the momentum recovery in the wake of aligned axial-flow hydrokinetic turbines, Phys. Fluids **34**, 105130 (2022).

[35] U. Ahmed, D. D. Apsley, I. Afgan, T. Stallard, and P. K. Stansby, Fluctuating loads on a tidal turbine due to velocity shear and turbulence: Comparison of CFD with field data, Renew. Energy **112**, 235 (2017).

[36] T. Stallard, H. Mullings, S. Draycott, and P. Ouro, Large-eddy simulations of interaction between surface waves and a tidal turbine wake in a turbulent channel, in *Proceedings of the 15th European Wave and Tidal Energy Conference (EWTEC '23)* (Bilbao, Spain, 2023).

[37] P. Ouro, L. Ramirez, and M. Harrold, Analysis of array spacing on tidal stream turbine farm performance using Large-Eddy Simulation, J. Fluids Struct. **91**, 102732 (2019).

[38] T. Stoesser, Physically realistic roughness closure scheme to simulate turbulent channel flow over rough beds within the framework of LES, J. Hydraul. Eng. **136**, 812 (2010).

[39] S. Kara, M. C. Kara, T. Stoesser, and T. W. Sturm, Free-surface versus rigid-lid LES computations for bridge-abutment flow, J. Hydraul. Eng. **141**, 04015019 (2015).

[40] P. Ouro, U. Lopez-Novoa, and M. F. Guest, On the performance of a highly-scalable computational fluid dynamics code on AMD, ARM and Intel processor-based HPC systems, Comput. Phys. Commun. **269**, 108105 (2021).

[41] M. Cevheri, R. McSherry, and T. Stoesser, A local mesh refinement approach for large-eddy simulations of turbulent flows, Int. J. Numer. Methods Fluids **82**, 261 (2016).

[42] P. Ouro, B. Fraga, U. Lopez-Novoa, and T. Stoesser, Scalability of an Eulerian-Lagrangian large-eddy simulation solver with hybrid MPI/OpenMP parallelisation, Comput. Fluids **179**, 123 (2019).

[43] A. Christou, Z. Xie, T. Stoesser, and P. Ouro, Propagation of a solitary wave over a finite submerged thin plate, Appl. Ocean Res. **106**, 102425 (2021).

[44] A. Christou, T. Stoesser, and Z. Xie, A large-eddy-simulation-based numerical wave tank for three-dimensional wave-structure interaction, Comput. Fluids **231**, 105179 (2021).

[45] R. Jalalabadi, T. Stoesser, P. Ouro, Q. Luo, and Z. Xie, Free surface flow over square bars at different Reynolds numbers, J. Hydro-Environ. Res. **36**, 67 (2021).

[46] K. V. Chua, B. Fraga, T. Stoesser, S. Ho Hong, and T. Sturm, Effect of bridge abutment length on turbulence structure and flow through the opening, J. Hydraul. Eng. **145**, 04019024 (2019).

[47] Q. Luo, G. Dolcetti, T. Stoesser, and S. Tait, Water surface response to turbulent flow over a backward-facing step, J. Fluid Mech. **966**, A18 (2023).

[48] R. McSherry, K. Chua, T. Stoesser, and S. Mulahasan, Free surface flow over square bars at intermediate relative submergence, J. Hydraul. Res. **56**, 825 (2018).

[49] Y. Liu, T. Stoesser, and H. Fang, Effect of secondary currents on the flow and turbulence in partially filled pipes, J. Fluid Mech. **938**, A16 (2022).

[50] C. Zhao, P. Ouro, T. Stoesser, S. Dey, and H. Fang, Response of flow and saltating particle characteristics to bed roughness and particle spatial density, Water Resour. Res. **150**, 1 (2022).

[51] V. I. Nikora, T. Stoesser, S. M. Cameron, M. Stewart, K. Papadopoulos, P. Ouro, R. McSherry, A. Zampiron, I. Marusic, and R. A. Falconer, Friction factor decomposition for rough-wall flows: Theoretical background and application to open-channel flows, J. Fluid Mech. **872**, 626 (2019).

[52] Y. Liu, T. Stoesser, H. Fang, A. Papanicolaou, and A. G. Tsakiris, Turbulent flow over an array of boulders placed on a rough, permeable bed, Comput. Fluids **158**, 120 (2017).

[53] Q. Luo, T. Stoesser, S. Cameron, V. Nikora, A. Zampiron, and W. Patella, Meandering of instantaneous large-scale structures in open-channel flow over longitudinal ridges, Environ. Fluid Mech. **23**, 829 (2023).

[54] P. Ouro, M. Harrold, T. Stoesser, and P. Bromley, Hydrodynamic loadings on a horizontal axis tidal turbine prototype, J. Fluids Struct. **71**, 78 (2017).

[55] P. Ouro and T. Stoesser, Impact of environmental turbulence on the performance and loadings of a tidal stream turbine, Flow Turbul. Combust. **102**, 613 (2019).

[56] P. Ouro and T. Nishino, Performance and wake characteristics of tidal turbines in an infinitely large array, J. Fluid Mech. **925**, A30 (2021).

[57] P. Ouro, H. Mullings, and T. Stallard, Establishing confidence in predictions of fatigue loading for floating tidal turbines based on large-eddy simulations andunsteady blade element momentum, in *Trends in Renewable Energies Offshore—Proceedings of the 5th International Conference on Renewable Energies Offshore (RENEW 2022)* (Lisbon, Portugal, 2023).

[58] H. Mullings, L. Amos, C. Miller, P. Ouro, and T. Stallard, Efficient prediction of tidal turbine fatigue loading using turbulent onset flow from Large Eddy Simulations (unpublished).

[59] R. Willden, X. Chen, S. Tucker Harvey, H. Edwards, C. Vogel, K. Bhavsar, T. Allsop, J. Gilbert, H. Mullings, M. Ghobrial, P. Ouro, D. Apsley, T. Stallard, I. Benson, A. Young, P. Schmitt, F. Zilic de Arcos, M.-A. Dufour, C. Choma Bex, G. Pinon, A. Evans, M. Togneri, I. Masters, L. da Silva Ignacio, C. Duarte, F. Souza, S. Gambuzza, Y. Liu, I. Viola, M. Rentschler, T. Gomes, G. Vaz, R. Azcueta, H. Ward, F. Salvatore, Z. Sarichloo, D. Calcagni, T. Tran, H. Ross, M. Olveira, R. R. Puraca, and B. Carmo, Tidal turbine benchmarking project: Stage I—Steady flow blind predictions, in *Proceedings of the 15th European Wave and Tidal Energy Conference (EWTEC '23)* (Bilbao, Spain, 2023).

[60] P. Ouro, P. K. Stansby, and T. Stallard, Analysis of the kinetic energy recovery behind a tidal stream turbine for various submergence levels, Int. Mar. Energy J. **5**, 265 (2022).

[61] P. Ouro, P. Stansby, A. Macleod, T. Stallard, and H. Mullings, High-fidelity modelling of a six-turbine tidal array in the Shetlands, in *Proceedings of the 15th European Wave and Tidal Energy Conference (EWTEC '23)* (Bilbao, Spain, 2023).

[62] T. Stoesser, Large-eddy simulation in hydraulics: Quo vadis? J. Hydraul. Res. **52**, 441 (2014).

[63] F. Nicoud and F. Ducros, Subgrid-scale stress modelling based on the square of the velocity, Flow Meas. Instrum. **62**, 183 (1999).

[64] M. Uhlmann, An immersed boundary method with direct forcing for the simulation of particulate flows, J. Comput. Phys. **209**, 448 (2005).

[65] S. Osher and J. A. Sethian, Fronts propagating with curvature-dependent speed: Algorithms based on hamilton-jacobi formulations, J. Comput. Phys. **79**, 12 (1988).

[66] M. Sussman, A level set approach for computing solutions to incompressible two-phase flow, J. Comput. Phys. **114**, 146 (1994).

[67] S. Kang and F. Sotiropoulos, Large-eddy simulation of three-dimensional turbulent free surface flow past a complex stream restoration structure, J. Hydraul. Eng. **141**, 04015022 (2015).

[68] N. Jarrin, S. Benhamadouche, D. Laurence, and R. Prosser, A synthetic-eddy-method for generating inflow conditions for large-eddy simulations, Int. J. Heat Fluid Flow **27**, 585 (2006).

[69] T. Stallard, T. Feng, and P. K. Stansby, Experimental study of the mean wake of a tidal stream rotor in a shallow turbulent flow, J. Fluids Struct. **54**, 235 (2015).

[70] P. Druault, B. Gaurier, and G. Germain, Spatial integration effect on velocity spectrum: Towards an interpretation of the -11/3 power law observed in the spectra of turbine outputs, Renew. Energy **181**, 1062 (2022).

[71] X. Yang, K. B. Howard, M. Guala, and F. Sotiropoulos, Effects of a three-dimensional hill on the wake characteristics of a model wind turbine, Phys. Fluids **27**, 025103 (2015).

[72] G. Cortina, M. Calaf, and R. B. Cal, Distribution of mean kinetic energy around an isolated wind turbine and a characteristic wind turbine of a very large wind farm, Phys. Rev. Fluids **1**, 074402 (2016).

[73] M. Bastankhah and F. Porté-Agel, A new analytical model for wind-turbine wakes, Renew. Energy **70**, 116 (2014).

[74] H. Tennekes and J. Lumley, *A First Course in Turbulence* (MIT Press, Cambridge, MA, 1978).